Stability and Localization of Rapid Shear in Fluid-Saturated Fault Gouge, 2. Localized zone width and strength evolution

John D. Platt[1], John W. Rudnicki[2,3], and James R. Rice[1,4]

Abstract. Field and laboratory observations indicate that at seismic slip rates most shearing is confined to a very narrow zone, just a few tens to hundreds of microns wide, and sometimes as small as a few microns. *Rice et al.* [2013] analyzed the stability of uniform shear in a fluid-saturated gouge material. They considered two distinct mechanisms to limit localization to a finite thickness zone, rate-strengthening friction and dilatancy. In this paper we use numerical simulations to extend beyond the linearized perturbation context in *Rice et al.* [2013], and study the behavior after the loss of stability. Neglecting dilatancy we find that straining localizes to a width that is almost independent of the gouge layer width, suggesting that the localized zone width is set by the physical properties of the gouge material. Choosing parameters thought to be representative of a crustal depth of 7 km, this predicts that deformation should be confined to a zone between 4 and 44 μm wide. Next, considering dilatancy alone we again find a localized zone thickness that is independent of gouge layer thickness. For dilatancy alone we predict localized zone thicknesses between 1 and 2 μm wide for a depth of 7 km. Finally we study the impact of localization on the shear strength and temperature evolution of the gouge material. Strain rate localization focuses frictional heating into a narrower zone, leading to a much faster temperature rise than that predicted when localization is not accounted for. Since the dynamic weakening mechanism considered here is thermally driven, this leads to accelerated dynamic weakening.

1. Introduction

Field and laboratory observations show evidence for micron-scale strain rate localization in fluid-saturated gouge materials sheared at seismic slip rates, as discussed in the introduction to the companion paper *Rice et al.* [2013]. Such extreme localization focuses the frictional heating into a narrow zone, making thermally driven dynamic weakening mechanisms such as thermal pressurization and thermal decomposition very efficient. This sensitive dependence of shear strength evolution on the width of the deforming zone can be seen in the calculations of *Rempel and Rice* [2006], *Noda et al.* [2009], *Sulem and Famin* [2009], and *Garagash* [2012].

The companion paper *Rice et al.* [2013] used a thermo-poro-mechanical model for deformation of a fluid-saturated gouge material to investigate the width of the deforming zone during rapid shear. In the absence of a stabilizing mechanism the deformation will collapse into a zone with zero width, as noted in *Rice* [2006]. Two stabilizing mechanisms were considered in *Rice et al.* [2013], frictional rate-strengthening and dilatancy. For each mechanism a linear stability analysis was used to determine when small deviations away from uniform straining of the gouge material will grow, and thus uniform straining will be unstable. For frictional rate-strengthening alone this led to a prediction for

the localized zone thickness as a function of the gouge properties. When localization is stabilized by dilatancy alone *Rice et al.* [2013] found a critical gouge layer thickness above which intense transient localization occurs at the onset of shear, although the strain rate perturbations eventually decay and shear is uniform at large slip.

In this paper we use numerical simulations to test the predictions of *Rice et al.* [2013]. We study how the properties of the gouge combine to set the localized zone thickness when nonlinear effects are accounted for, and compare this with the formula predicted in *Rice et al.* [2013]. We also study how the development of a localized shear zone influences the maximum temperature rise and shear strength evolution, showing that the development of a localized zone corresponds to a sudden strength drop.

2. Model formulation

In this section we outline the model for deformation of a fluid-saturated gouge material. A more detailed development of the model can be found in the companion paper, *Rice et al.* [2013]. We consider a gouge layer with a finite thickness h confined between two poroelastic half-spaces being moved relative to each other at a slip rate V. The model is one-dimensional and we only account for spatial variations that depend on the coordinate perpendicular to the slip direction, y. All values of y are measured relative to the line $y = 0$ at the center of the gouge layer. A sketch of this system is shown in Figure 1.

2.1. Mechanical equilibrium

Rice [2006] hypothesized that, due to the small lengths that diffusion of heat and pore fluid act over, unrealistically high accelerations are required to make inertial effects important within the gouge layer. Motivated by this we neglect inertia within the gouge layer, leaving us with the conditions for mechanical equilibrium,

$$\frac{\partial \tau}{\partial y} = 0 \quad , \quad \frac{\partial \sigma_n}{\partial y} = 0 \tag{1}$$

[1]School of Engineering and Applied Sciences, Harvard University, Cambridge, Massachusetts, USA.

[2]Department of Mechanical Engineering, Northwestern University, Evanston, Illinois, USA.

[3]Department of Civil and Environmental Engineering, Northwestern University, Evanston, Illinois, USA.

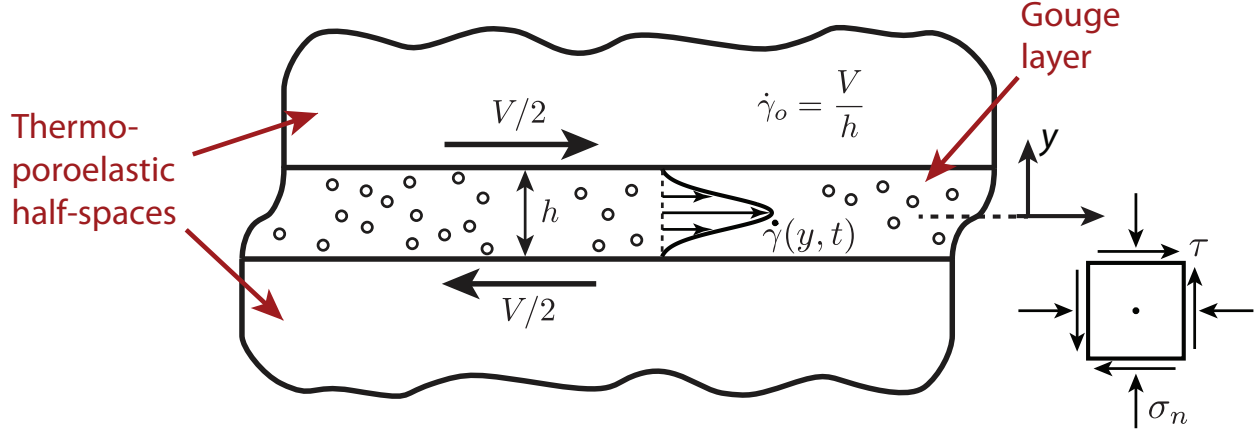[4]Earth and Planetary Sciences, Harvard University, Cambridge, Massachusetts, USA.

Figure 1. A sketch showing the system we are modeling. A gouge layer with a finite thickness h is sheared between two rigid poroelastic half-spaces that are moved relative to each other at a slip rate V. This leads to a nominal strain rate within the gouge layer $\dot{\gamma}_o = V/h$. The strain rate $\dot{\gamma}(y,t)$ will localize within the gouge layer, as shown by the Gaussian strain rate profile sketched within the gouge layer. The width W of the zone of localized straining is then estimated as twice the root mean square width of the Gaussian.

where τ is the shear stress in the layer, σ_n is the compressive stress normal to the fault. This means that the stresses in the layer are at most a function of time, t. We assume that the normal stress does not evolve with time, and thus σ_n is constant. Later in this paper we determine when inertial effects will significantly alter our results. The shear stress is taken to be the product of the effective stress and a friction coefficient f,

$$\tau = f(\sigma_n - p), \qquad (2)$$

where p is the local pore pressure.

2.2. Gouge friction

Constructing friction laws appropriate for the high deformation rates considered here is difficult due to the complex interplay between purely frictional, temperature and pore fluid effects. In the absence of such a friction law we use,

$$f(\dot{\gamma}) = (a - b) \sinh^{-1}\left[\frac{\dot{\gamma}}{2\dot{\gamma}_o} \exp\left(\frac{f_o}{a - b}\right)\right], \qquad (3)$$

which for $(a-b) \ll f_o$ is asymptotically the same as the friction law for steady state shearing inferred from low strain rate velocity-stepping experiments such as those in *Dieterich* [1979],

$$f = f_o + (a - b) \log\left(\frac{\dot{\gamma}}{\dot{\gamma}_o}\right). \qquad (4)$$

Here f_o is the friction coefficient at the reference strain rate $\dot{\gamma}_o$, and $(a - b)$ quantifies the change in friction with strain rate. We will assume that the gouge is rate-strengthening, and thus $(a - b) > 0$. We use the regularized friction law in equation (3) instead of the logarithmic friction law in equation (4) to avoid difficulties when $\dot{\gamma} \to 0$.

Since the shear stress is at most a function of t, combining equations (2) and (3) we can see high pore pressures will correspond to high values of $\dot{\gamma}$. Equation (3) is a simplification of reality, and neglects temperature, state evolution and mineralogical effects. An expanded discussion of the assumptions implicit in using steady state friction laws that depend on strain rate alone can be found in *Rice et al.* [2013].

2.3. Conservation of energy

Following [*Rice et al.*, 2013] the conservation of energy is written as

$$\frac{\partial T}{\partial t} = \frac{\tau\dot{\gamma}}{\rho c} + \alpha_{th}\frac{\partial^2 T}{\partial y^2}, \qquad (5)$$

where T is temperature, α_{th} is the thermal diffusivity, and ρc is the effective heat capacity per unit volume in the reference state. Both ρc and α_{th} are taken to be constant. Since the shear stress τ is constant throughout the gouge layer, frictional heating will be focused in regions of high strain rate. Diffusion will then transport this heat into the adjacent material.

2.4. Conservation of pore fluid

As shown in *Rice et al.* [2013], conservation of pore fluid mass leads to,

$$\frac{\partial p}{\partial t} = \Lambda\frac{\partial T}{\partial t} - \frac{\varepsilon}{\beta\dot{\gamma}}\frac{\partial\dot{\gamma}}{\partial t} + \alpha_{hy}\frac{\partial^2 p}{\partial y^2}, \qquad (6)$$

The first term on the right hand side of equation (6) represents thermal pressurization. As the pore fluid is heated it will expand, and if the gouge is undrained or partially drained this thermal expansion will lead to a pore pressure increase. The parameter Λ is defined as,

$$\Lambda = \frac{\lambda_f - \lambda_n}{\beta_f + \beta_n}, \qquad (7)$$

where β_n and λ_n are the compressibility and the thermal expansivity of the pore volume, β_f and λ_f are the compressibility and the thermal expansivity of the pore fluid, and the instantaneous pore pressure change accompanying a temperature change ΔT is $\Delta p = \Lambda\Delta T$. The second term in equation (6) models pore pressure decreases due to gouge dilatancy. Our model for dilatancy is based on the work of *Segall and Rice* [1995], which assumes that changes of inelastic porosity are a result of changes in strain rate. ε quantifies the magnitude of dilatancy and β is the storage capacity of the gouge. The final term in equation (6) represents hydraulic diffusion and, for simplicity, we have assumed that the hydraulic diffusivity α_{hy} is constant.

2.5. Nondimensional parameters

Now we determine the dimensionless parameters for this system of equations. The scalings used are based upon the geometry of the gouge layer and the solution for a uniformly sheared gouge layer developed by *Lachenbruch* [1980], discussed in more detail in Section 4 and in *Rice et al.* [2013].

Table 1. Representative parameters modeling a depth of 7 km. A fuller discussion on the origin of the parameters is included in *Rice et al.* [2013].

Parameter	Intact material, nominal values	Intact material, path-averaged values	Damaged material, nominal values	Damaged material, path-averaged values
α_{th}, mm^2/s	0.7	0.66	0.7	0.54
ρc, MPa/K	2.7	2.7	2.7	2.7
Λ, MPa/K	0.93	0.89	0.31	0.30
α_{hy}, mm^2/s	0.86	2.05	3.52	6.71
β, $\times 10^{-10}$ Pa^{-1}	0.52	0.55	1.26	2.97
ε	1.7×10^{-4}	1.7×10^{-4}	1.7×10^{-4}	1.7×10^{-4}
$\sigma_n - p_a$, MPa	126	126	126	126
ρ, kg/m^3	2800	2800	2800	2800

First, the gouge layer width h is used to scale y. The gouge layer of thickness h can then be combined with slip rate V to find the nominal strain rate $\dot{\gamma}_o = V/h$ for the gouge layer. This nominal strain rate is used to scale $\dot{\gamma}$. The nominal strain rate is combined with the critical weakening strain for thermal pressurization $\gamma_w = \rho c/f_o\Lambda$ to get the characteristic weakening timescale $t_w = \gamma_w/\dot{\gamma}_o$ for thermal pressurization, which is used to scale t. Finally, we use the ambient effective stress $\bar{\sigma}_a$ to scale the pore pressure variations, and the total temperature rise from the uniform solution $\bar{\sigma}_a\Lambda$ to scale the temperature variations. To summarize,

$$y = hy' \quad , \quad t = \frac{\rho ch}{f_o\Lambda V}t' \quad , \quad \dot{\gamma} = \dot{\gamma}_o\dot{\gamma}' \qquad (8)$$

$$p = p_a + (\sigma_n - p_a)p' \quad , \quad T = T_a + \frac{\sigma_n - p_a}{\Lambda}T'$$

where p_a and T_a are the ambient pore pressure and temperature of the material, and the primed variables are dimensionless.

The above scalings leads to the set of dimensionless equations,

$$\frac{\partial T'}{\partial t'} = \tau'\dot{\gamma}' + D_{th}\frac{\partial^2 T'}{\partial y'^2}, \qquad (9a)$$

$$\frac{\partial p'}{\partial t'} = \frac{\partial T'}{\partial t'} - \frac{E}{\dot{\gamma}'}\frac{\partial \dot{\gamma}'}{\partial t'} + D_{hy}\frac{\partial^2 p'}{\partial y'^2}, \qquad (9b)$$

$$\frac{\partial \tau'}{\partial y'} = 0, \qquad (9c)$$

$$\tau = f(\dot{\gamma}')(1 - p'), \qquad (9d)$$

$$f(\dot{\gamma}') = 1 + z^{-1}\log\dot{\gamma}'. \qquad (9e)$$

Despite the large number of parameters in our model, there are only four dimensionless parameters,

$$D_{th} = \frac{\alpha_{th}\rho c}{f_o\Lambda Vh} \quad , \quad D_{hy} = \frac{\alpha_{hy}\rho c}{f_o\Lambda Vh}, \qquad (10)$$

$$z = \frac{f_o}{a - b} \quad , \quad E = \frac{\varepsilon}{\beta\bar{\sigma}_a}.$$

All of the parameters in our problem affect the response only in so far they affect these four dimensionless parameters. D_{th} and D_{hy} measure the strength of thermal and hydraulic diffusion respectively, z measures the rate-strengthening component of friction, and E quantifies the strength of dilatancy.

The parameters D_{th} and D_{hy} can be better understood by rewriting them as,

$$D_{th} = \left(\frac{L_{thd}}{4\pi^2 h}\right)^2 \quad , \quad D_{hy} = \left(\frac{L_{hyd}}{4\pi^2 h}\right)^2, \qquad (11)$$

where L_{thd} and L_{hyd} are the distances over which diffusion acts for a timescale comparable to the characteristic weak-

ening timescale for thermal pressurization,

$$L_{thd} = 2\pi\sqrt{\alpha_{th}t_w} \quad , \quad L_{hyd} = 2\pi\sqrt{\alpha_{hy}t_w}. \qquad (12)$$

This means that small values of D_{th} and D_{hy} correspond to diffusion distances much smaller than the gouge layer thickness, allowing for the possibility of steep gradients in p and T across the gouge layer.

3. Parameter values

The hydraulic parameters α_{hy}, Λ and β are the least constrained in the model, and are expected to vary with temperature, pore pressure and damage to the gouge and surrounding material. In this paper we will consider one class of hydraulic parameters modeling a depth of 7 km, a typical centroidal depth for crustal earthquakes, and another class of hydraulic parameters modeling a depth of 1 km, a typical depth for boreholes drilled through active fault zones. Within each class of parameters we use the methods outlined in *Rice* [2006] to account for parameters variations due to damage, as well as pore pressure and temperature changes.

To model a depth of 7 km we use the four parameter sets from *Rempel and Rice* [2006], which are based on Tables 1-3 in *Rice* [2006] and the procedures in *Rice* [2006]. Damage of the gouge by inelastic shear and fresh micro-cracking may occur in the concentrated stress field at the tip of a propagating rupture. This damage is modeled, somewhat arbitrarily,

Table 2. Two parameters sets intended to model a depth of 1 km, a typical intersection depth for boreholes drilled through active faults. Parameter variations due to pore pressure and temperature changes are neglected, so all parameters are evaluated at the ambient conditions $p_a = 10$ MPa, $\sigma_n = 28$ MPa and $T_a = 30$ °C. Damage is modeled by increasing the permeability by a factor of ten and the drained compressibility by a factor of two, as suggested in *Rice* [2006]. Sources for the parameter values are outlined in the text and include *Fine and Millero* [1973], *Wibberley and Shimamoto* [2003], and *Likhachev* [2003].

Parameter	Intact material	Damaged material
n	0.068	0.068
β_f, $\times 10^{-9}$ Pa^{-1}	0.44	0.44
β_n, $\times 10^{-9}$ Pa^{-1}	1.53	6.01
λ_f, $\times 10^{-4}$K^{-1}	3.11	3.11
λ_n, $\times 10^{-4}$K^{-1}	-1.36	-1.36
η_f, $\times 10^{-4}$ Pa s	7.97	7.97
k, $\times 10^{-19}$ m^2	2.5	25
α_{th}, mm^2/s	0.7	0.7
ρc, MPa/K	2.7	2.7
Λ, MPa/K	0.22	0.068
α_{hy}, mm^2/s	2.34	7.15
β, $\times 10^{-10}$ Pa^{-1}	1.34	4.39
ε	1.7×10^{-4}	1.7×10^{-4}
$\sigma_n - p_a$, MPa	18	18
ρ, kg/m^3	2800	2800

by increasing the permeability by an order of magnitude and the drained compressibility by a factor of two, as suggested in *Rice* [2006]. Parameter variations due to temperature and pore pressure changes are either neglected by evaluating the parameters at the ambient conditions, leading to the nominal parameter sets, or accounted for by averaging along an expected p-T path, leading to the path-averaged parameter sets. The four parameter sets are summarized in Table 1 and are discussed in more detail in *Rice et al.* [2013].

Next we develop parameters modeling a depth of 1 km. No attempt is made to account for the effects of pore pressure and temperature changes and all parameters are evaluated at the ambient conditions $p_a = 10$ MPa, $\sigma_n = 28$ MPa and $T_a = 30$ °C. As before damage is accounted for using the procedure from *Rice* [2006]. The gouge properties are determined using the data from *Wibberley and Shimamoto* [2003]. We infer a porosity of $n = 0.068$, and a pore volume thermal expansion coefficient $\lambda_n = -1.36 \times 10^{-4}$ °C^{-1}. For an intact material the pore volume compressibility is $\beta_n = 1.53 \times 10^{-9}$ Pa^{-1}, and for a damaged material $\beta_n = 6.01 \times 10^{-9}$ Pa^{-1}. To estimate the permeability we assume a maximum burial depth of 4-5 km, we find a permeability of $\sim 2.5 \times 10^{-19}$ m^2 for intact material. As suggested in *Rice* [2006] this value is increased by a factor of ten to model a damaged material. Next we consider the pore fluid properties. *Fine and Millero* [1973] used sound speed data to calculate the compressibility and thermal expansion coefficient of pure water as a function of pressure and temperature, leading to $\beta_f = 0.44 \times 10^{-9}$ Pa^{-1} and $\lambda_f = 3.11 \times 10^{-4}$ °C^{-1}. Finally *Likhachev* [2003] provides a formula for the viscosity of water for a temperature range of 273-463 K and a pressure range of 1-250 bar. Using this we calculate $\eta_f = 7.97 \times 10^{-4}$ Pa s. These parameter sets are summarized in Table 2.

The parameter sets in Tables 1 and 2 show that damaged material, when modeled as in *Rice* [2006], is characterized by higher values of α_{hy} and β, and lower values of Λ. This means that thermal pressurization and dilatancy will be less

Figure 3. Rate-strengthening friction: A plot showing the strain rate profile at peak localization for the path-averaged parameters modeling a damaged material, $V = 1$ m/s and $h = 1$ mm. The numerical solution is shown in blue with the Gaussian fit defined by equation (27) shown by the red dashed line. The width W_{rsf} of the localized zone is estimated as twice the root mean square width of the Gaussian, and we find $W_{rsf} = 43$ μm.

efficient in a damaged material, while hydraulic diffusion will be more efficient. Comparing the nominal parameter sets modeling a depth of 1 km and 7 km we see the same pattern, with more efficient thermal pressurization and dilatancy expected at 7 km than at 1 km and less efficient hydraulic diffusion.

Compared with the hydraulic parameters, the thermal parameters are well constrained. The effective heat capacity per unit volume is $\rho c = 2.7$ MPa °C^{-1} [*Lachenbruch*, 1980; *Mase and Smith*, 1987], and *Rice* [2006] quotes a range for α_{th} of 0.5 to 0.7 mm^2/s. We choose a value of 0.7 mm^2/s for the nominal parameter sets, and use the values for α_{th} given in *Rempel and Rice* [2006] for the path-averaged parameter sets. The thermal parameters are assumed to not change with depth. In reality there will be some variation with depth, but we implicitly assume that changes in the thermal parameters are negligible when compared with the depth variation of the hydraulic parameters.

The logarithmic friction law used in this paper is taken from experiments performed at slip rates on the order of 1-10 μm/s, and thus equation (3) may not accurately describe gouge friction at the seismic slip rates considered in this paper. However, current high-velocity friction experiments are unable to separate the frictional response from temperature and pore fluid effects to provide a formula for the friction coefficient valid at the deformation rates considered here. As in *Rice et al.* [2013] we choose $f_o = 0.6$ and $(a - b) = 0.025$ motivated by the measurements for granite under hydrothermal conditions in *Blanpied et al.* [1998], though the results are presented in a form that allows predictions for a range of f_o and $(a - b)$. A larger discussion of the simplifications associated with equation (3) can be found in the companion paper *Rice et al.* [2013].

4. End-member solutions

In this section we discuss two end-member solutions for dynamic weakening driven by thermal pressurization. To do this we compare the hydrothermal diffusion distance $\sqrt{4\alpha t}$
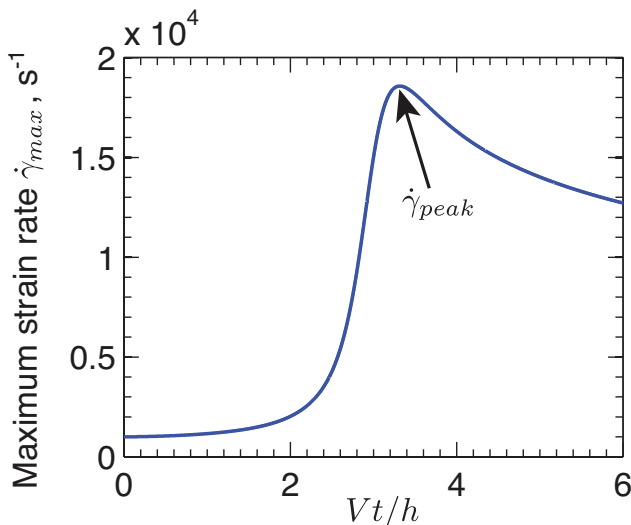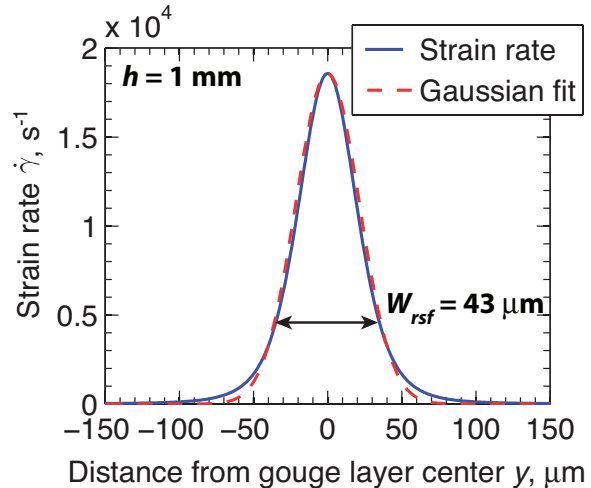

Figure 2. Rate-strengthening friction: The blue curve shows the evolution of the maximum strain rate $\dot{\gamma}_{max}$ within the gouge layer for the path-averaged parameters modeling a damaged material, $V = 1$ m/s and $h = 1$ mm. The maximum strain rate grows indicating that straining is localizing within the gouge layer. After a finite amount of slip the peak strain rate begins to decay indicating that the localized zone is thickening. This thickening occurs whenever both α_{th} and α_{hy} are non-zero. We define the peak strain rate $\dot{\gamma}_{peak}$ to be the largest value of $\dot{\gamma}_{max}$.

with the gouge layer width h, where we define the lump hydrothermal diffusivity as

$$\alpha = \left(\sqrt{\alpha_{th}} + \sqrt{\alpha_{hy}} \right)^2. \tag{13}$$

During the initial stages of deformation the hydrothermal diffusion distance will be much smaller than the width of the gouge layer, $\sqrt{4\alpha t} \ll h$. This means that deformation is effectively undrained and adiabatic, the limit studied in *Lachenbruch* [1980] when the constant dilatational strain rate assumed in *Lachenbruch* [1980] is zero. *Lachenbruch* [1980] solved for the strength evolution

$$\tau = f_o \bar{\sigma}_a \exp \left(-\frac{f_o \Lambda}{\rho c} \dot{\gamma}_o t \right). \tag{14}$$

Thermal pressurization leads to an exponentially decaying shear stress, and the weakening shear strain associated with thermal pressurization is,

$$\gamma_w = \frac{\rho c}{f_o \Lambda}. \tag{15}$$

The weakening timescale, which was used earlier to nondimensionalize t, is then the ratio of the weakening strain and strain rate, $t_w = \gamma_w / \dot{\gamma}_o$. Since the system is controlled by a critical strain, the slip-weakening distance $h\gamma_w$ scales linearly with the width of the deforming zone. *Lachenbruch* [1980] also solved for T in the undrained and adiabatic limit, finding

$$T - T_a = \frac{\bar{\sigma}_a}{\Lambda} \left[1 - \exp \left(-\frac{\dot{\gamma}_o t}{\gamma_w} \right) \right] \tag{16}$$

where T_a is the ambient temperature. The dynamic weakening associated with thermal pressurization leads to a finite temperature rise of $\bar{\sigma}_a / \Lambda$ and the critical weakening strain γ_w also controls the approach of T to the maximum temperature.

At very large displacements the diffusion distance will be much larger than the gouge layer width, $\sqrt{4\alpha t} \gg h$. In this limit the finite thickness of the gouge layer will be negligible, and deformation can be approximated by slip on a mathematical plane. This problem was solved for a uniform slip rate V by *Mase and Smith* [1985, 1987] for the special case of an immobile pore fluid (i.e $\alpha_{hy} = 0$). The more general solution was found by Rice [2006], for the case of non-zero α_{hy}, which in the end involved no more than replacing α_{th} in their result for $\tau(t)$ with the lump hydrothermal diffusivity α defined above in equation (13), leading to the shear strength evolution

$$\tau = f_o \bar{\sigma}_a \exp \left(\frac{Vt}{L^*} \right) \text{erfc} \left(\sqrt{\frac{Vt}{L^*}} \right), \tag{17}$$

where

$$L^* = \frac{4\alpha}{V} \left(\frac{\rho c}{f_o \Lambda} \right)^2. \tag{18}$$

This solution had been recognized by *Mase and Smith* [1987], in the case of thermal diffusion only, as a limiting result for a narrow shear zone. The weakening slip distance L^* is set by the weakening strain γ_w and the lengthscale defined by the hydrothermal diffusivity α and the slip rate V. The corresponding solution for slip surface temperature is,

$$T - T_a = \frac{\bar{\sigma}_a}{\Lambda} \left(1 + \sqrt{\frac{\alpha_{hy}}{\alpha_{th}}} \right) \left[1 - \exp \left(\frac{Vt}{L^*} \right) \text{erfc} \left(\sqrt{\frac{Vt}{L^*}} \right) \right]. \tag{19}$$

Again we see that thermal pressurization leads to a finite temperature rise, and the lengthscale that controls the tem-

perature evolution is the same length that controls the shear strength evolution. We shall refer to the *Rice* [2006] solution in equations (17)-(19) as the Mase-Smith-Rice slip on a plane solution.

Rempel and Rice [2006] showed that the two limits considered above are the end-member solutions for a gouge layer sheared uniformly between two conducting half-spaces. We will investigate how strain rate localization alters the results of *Rempel and Rice* [2006], and how the solutions with localization relate to these two end-member solutions.

5. Frictional rate-strengthening only

5.1. Linear stability results

Initially we consider a system in which dilatancy is neglected, and thus $\varepsilon = 0$. *Rice et al.* [2013] determined the stability of the uniform shearing solution presented in *Lachenbruch* [1980]. Linearizing about this solution led to a relationship between the wavelength λ of a perturbation in p and T and the growth rate s, in an $\exp(st)$ form, given by,

$$\frac{z\dot{\gamma}_o}{\gamma_w} s = \left(s + \frac{4\pi^2 \alpha_{th}}{\lambda^2} \right) \left(s + \frac{4\pi^2 \alpha_{hy}}{\lambda^2} \right). \tag{20}$$

Separating the growth rate into real and imaginary components, $s = s_R(\lambda) + s_I(\lambda)$, we determine the critical wavelength λ_{pT} that separates growing and decaying perturbations in p and T is

$$\lambda_{pT} = 2\pi \sqrt{\frac{\alpha_{th} + \alpha_{hy}}{z(\dot{\gamma}_o / \gamma_w)}}. \tag{21}$$
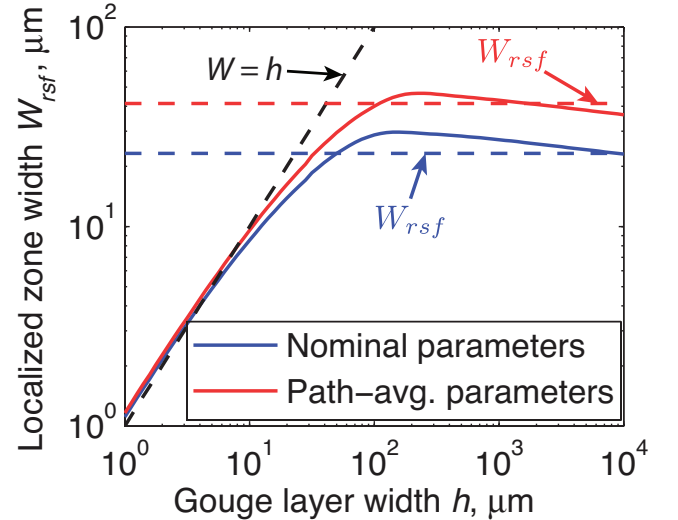

Figure 4. Rate-strengthening friction: Figure showing how the localized zone thickness W_{rsf} at peak localization depends on gouge layer thickness h. Numerical results for the path-averaged and nominal parameters for a damaged material and a slip rate of $V = 1$ m/s are shown by solid colored lines, with the accompanying linear stability predictions for these parameters shown by dashed colored line. For thin gouge layers we see that the localized zone thickness is equal to the gouge layer thickness, with the line $W = h$ shown by dashed black line for guidance. When the gouge layer thickness is large the straining localizes to a width that is only weakly dependent on the gouge layer thickness. This width is in good agreement with the predictions for W_{rsf} from the linear stability analysis in *Rice et al.* [2013].
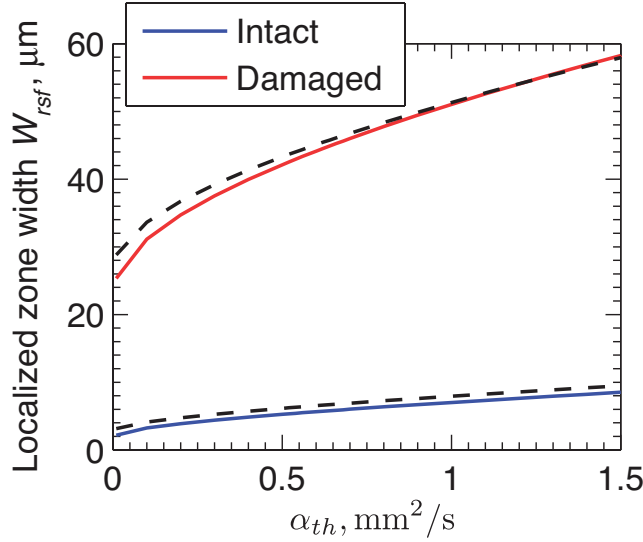
Figure 5. Rate-strengthening friction: A plot showing how the localized zone thickness W_{rsf} changes with α_{th} for the path-averaged parameters modeling an intact material and a damaged material given in Table 1, a slip rate $V = 1$ m/s and gouge layer thickness $h = 1$ mm. This parameter sweep allows us to vary the dimensionless parameter D_{th} while the other two dimensionless parameters D_{hy} and z remain unchanged. The black dashed lines show the fitting formula given in equation (31). Larger values of α_{th} lead to wider localized zones.

Figure 6. Rate-strengthening friction: A plot showing how the localized zone thickness W_{rsf} changes with α_{hy} for the path-averaged parameters modeling an intact material and a damaged material given in Table 1, a slip rate $V = 1$ m/s and gouge layer thickness $h = 1$ mm. This parameter sweep allows us to vary the dimensionless parameter D_{hy} while the other two dimensionless parameters D_{th} and z remain unchanged. The black dashed lines show the fitting formula given in equation (31). Larger values of α_{hy} lead to wider localized zones. The deviation at large values of α_{hy} for the damaged parameter set is due to W_{rsf} becoming comparable to h.

For $\lambda > \lambda_{pT}$ perturbations in p and T will grow unstably, while for $\lambda < \lambda_{pT}$ they will decay. Perturbations in strain rate are proportional to $\exp((s + \dot{\gamma}_o/\gamma_w)t)$ so we can define a similar critical wavelength,

$$\lambda_{shr} = 2\pi \sqrt{\frac{\alpha_{th} + \alpha_{hy}}{(z+2)(\dot{\gamma}_o/\gamma_w)}}, \qquad (22)$$

which separates growing and decaying perturbations in strain rate. For $\lambda > \lambda_{shr}$ strain rate perturbations will grow, leading to strain localization.

The critical wavelengths outlined above depend on the nominal strain rate $\dot{\gamma}_o$, which depends on the width of the deforming zone. *Rice et al.* [2013] turned the critical wavelength (22) into an approximate prediction for the localized zone thickness W_{rsf}, as controlled by rate-strengthening friction, by setting,

$$W_{rsf} = \frac{\lambda_{shr}}{2} \quad \text{with} \quad \dot{\gamma}_o = \frac{V}{W_{rsf}}. \qquad (23)$$

This leads to a prediction for the localized zone thickness that depends only on the gouge properties and the slip rate V,

$$W_{rsf} = \frac{\pi^2 \rho c}{f_o \Lambda (z+2)} \frac{\alpha_{hy} + \alpha_{th}}{V}. \qquad (24)$$

The localized thickness is set by a balance between frictional rate-strengthening, thermal pressurization and hydrothermal diffusion.

5.2. Localized zone thickness

Now we solve numerically for a finite thickness gouge layer sheared between two poroelastic half-spaces, the geometry shown in Figure 1, to see how the linear stability prediction matches the behaviour of the full nonlinear system. The poroelastic half-spaces do not deform and conduct heat and
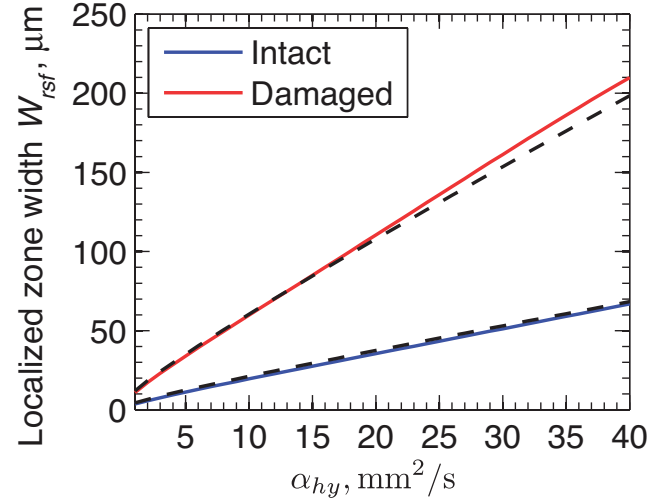
pore fluid away from the gouge layer. We assume that the transport properties of the half-spaces are the same as those of the gouge material. For initial conditions we set pressure and temperature to the ambient values $p_a = 70$ MPa and $T_a = 210$ °C, and assumes that the gouge begins shearing uniformly with $\dot{\gamma} = \dot{\gamma}_o$. Interestingly the three dimensionless parameters that control this system are independent of the ambient pore pressure and temperature. The additional constraint imposed to solve for τ,

$$\int_{-h/2}^{h/2} \dot{\gamma}(y,t)\mathrm{d}y = V, \qquad (25)$$

assures that the total straining within the gouge layer is equal to the slip rate V imposed across the gouge layer, as shown in Figure 1. This means that the average strain rate within the layer is equal to the nominal strain rate $\dot{\gamma}_o = V/h$.

Using the path-averaged parameters for a damaged material (see Table 1) we now solve for a gouge layer thickness $h = 1$ mm and a slip rate $V = 1$ m/s, justified as an average earthquake slip rate in *Rice et al.* [2013]. For this parameter set the linear stability prediction for the localized zone thickness is $W = 41$ μm, over an order of magnitude smaller than the gouge layer thickness. This leads us to expect significant strain rate localization to occur.

To visualize the evolution of strain rate localization we plot the maximum strain rate in the gouge layer,

$$\dot{\gamma}_{max}(t) = \max_y [\dot{\gamma}(y,t)], \qquad (26)$$

as a function of time. Since the total straining accommodated across the gouge layer is fixed at $\dot{\gamma}_o$ a larger value of $\dot{\gamma}_{max}$ corresponds to a narrower deforming zone. Figure 2 shows how the maximum strain rate within the gouge layer evolves with time. Initially the maximum strain rate grows

to values over an order of magnitude greater than the nominal strain rate $\dot{\gamma}_o$ showing that, as expected, straining is localizing within the gouge layer. Eventually $\dot{\gamma}_{max}$ reaches a peak value and begins to decay. This means that the thickness of the deforming zone, which initially will be the width of the gouge layer, gradually decreases to a narrowest value before widening again. Two additional instabilities exist that lead to movement of the localized straining zone across the gouge layer and these prevent the maximum strain rate decaying all the way back to uniform straining. These instabilities are not discussed here but will be the focus of future work.

Having described the temporal evolution of the maximum strain rate within the layer we next look at the spatial distribution of straining. The blue curve in Figure 3 shows the strain rate profile at peak localization, where peak localization is the point at which $\dot{\gamma}_{max}$ reaches its maximum value. The shape of the strain rate curve leads us to try to fit $\dot{\gamma}$ using the Gaussian function,

$$\dot{\gamma}_{fit} = A + B \exp\left(-\frac{2y^2}{W_{rsf}^2}\right). \tag{27}$$

This provides an excellent fit to the numerical solution as shown by the dashed red curve in Figure 3. To determine the three constants A, B and W_{rsf} we impose three conditions; $\dot{\gamma}_{fit}$ matches the numerical solution for $\dot{\gamma}$ at the centre of the gouge layer, the edge of the gouge layer, and accommodates the right amount of straining,

$$\int_{-h/2}^{h/2} \dot{\gamma}_{fit}(y,t)\mathrm{d}y = V. \tag{28}$$

This fitting formula gives us an objective way to measure the width of the zone of localized straining, allowing a comparison with the linear stability predictions. The constant A is included to allow us to fit straining profiles that have a width comparable to the gouge layer thickness. When
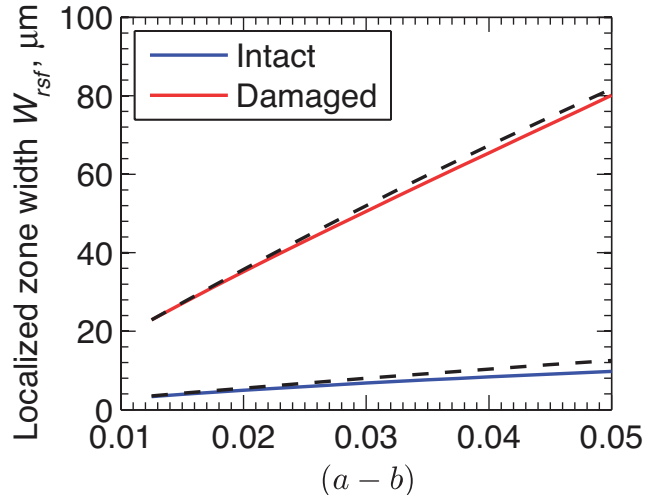

Figure 7. Rate-strengthening friction: A plot showing how the localized zone thickness W_{rsf} changes with $(a-b)$ for the path-averaged parameters modeling an intact material and a damaged material given in Table 1, a slip rate $V = 1$ m/s and gouge layer thickness $h = 1$ mm. This parameter sweep allows us to vary the dimensionless parameter z while the other two dimensionless parameters D_{hy} and D_{th} remain unchanged. The black dashed lines show the fitting formula given in equation (31). Larger values of $(a-b)$ lead to wider localized zones.
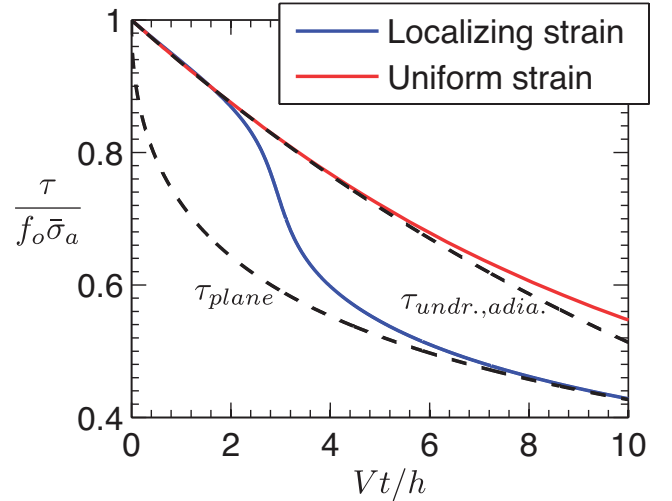

Figure 8. Rate-strengthening friction: A plot showing how the strength of the gouge layer evolves, normalized by the initial strength, for localizing shear and uniform shear. These simulations were produced using the path-averaged parameters modeling a damaged material, $V = 1$ m/s and $h = 1$ mm. We see that a sudden drop in strength coincides with the onset of localization. The initial deformation, before diffusion and localization have had time to act, is well described by the solution for uniform shear under undrained and adiabatic condition [*Lachenbruch*, 1980] . At large slips the solution is no longer influenced by the small yet finite width of the shearing zone and the strength is well approximated by the solution for slip on a plane [*Mase and Smith*, 1987; *Rice*, 2006]. The two limits for undrained adiabatic deformation and slip on a plane are shown above by the dashed black lines. Note that the undrained adiabatic solution from *Lachenbruch* [1980] differs from our simulation of a uniformly sheared layer because our numerical simulations allow for diffusion of heat and fluid into the surroundings.

straining is localized A becomes negligible and our fitting function becomes equivalent to the Gaussian straining profile previously used in models of thermal pressurization, for example *Andrews* [2002], *Rempel and Rice* [2006],*Noda et al.* [2009], and *Garagash* [2012]. For this limit where A is negligible we can calculate W_{rsf} using the formula,

$$W_{rsf} = \sqrt{\frac{2}{\pi}} \frac{V}{\dot{\gamma}_{peak}}, \tag{29}$$

where we have defined the peak strain rate

$$\dot{\gamma}_{peak} = \max_{t,y} \left[\dot{\gamma}(y,t)\right]. \tag{30}$$

For the rate-strengthening friction simulation shown in 3 we find $W_{rsf} = 43$ μm, in good agreement with the linear stability prediction of 41 μm. While Figure 3 only shows a snapshot of the strain rate profile, the Gaussian function above provides an excellent fit to the numerical solutions throughout the evolution of the localized zone.

Next we see how the width of the gouge layer influences the width of the localized zone. Figure 4 shows the localized zone thickness at peak localization found using the gaussian fit versus gouge layer thickness for the nominal and path-averaged parameters modeling a damaged material, $h = 1$ mm and $V = 1$ m/s. We see two distinct regimes. For thin
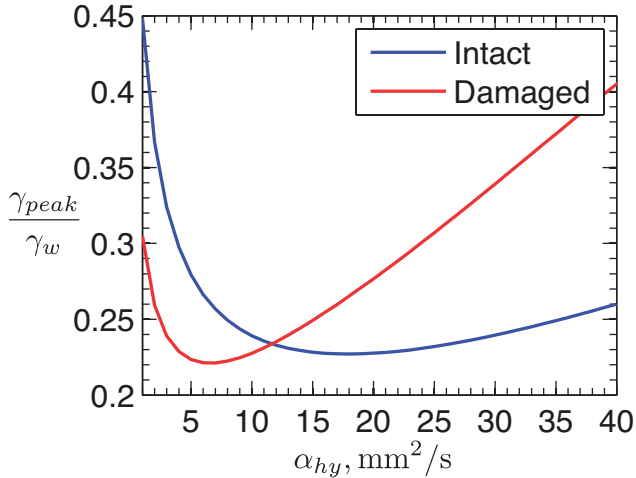
Figure 9. Rate-strengthening friction: A plot showing how the nominal strain at which peak localization occurs varies with α_{hy}. These simulations were produced using the path-averaged parameters for an intact and a damaged material, $V = 1$ m/s and $h = 1$ mm. For low values of α_{hy}, corresponding to localized zone thicknesses that are much smaller than the gouge layer thickness, the critical strain is a decreasing function of α_{hy}. For both parameter sets γ_{peak} reaches a minimum before increasing at large values of α_{hy}.

Figure 10. Rate-strengthening friction: A plot showing how the nominal strain at which peak localization occurs varies with α_{hy}. These simulations were produced using the path-averaged parameters for an intact and a damaged material, $V = 1$ m/s and $h = 1$ mm. We see that small values of $(a-b)$ lead to small values of γ_{peak}, and so the more intense localized zones also develop the fastest.

gouge layers $W_{rsf} \approx h$, corresponding to a gouge layer that is too narrow to allow straining to localize. However, once the gouge layer width exceeds a critical value the straining begins to localize, shown by the two curves falling beneath the line $W = h$. Once h exceeds this critical width the localized zone thickness is almost independent of h, changing by just twenty percent while h changes by three orders of magnitude. The linear stability predictions, shown by the colored dashed lines in Figure 4, provide reasonable agreement with the widths observed in the numerical simulations. It is encouraging that the linear stability prediction, which is taken infinitesimally close to uniform shearing, agrees so well with the localized zone thickness inferred at peak localization.

Next we perform a parameter sweep to determine how W_{rsf} depends on the gouge properties, implicitly assuming that the weak dependence of h is unimportant and the localized zone thickness is set by the gouge properties. As shown in Subsection 2.5, when dilatancy is neglected, there are just three dimensionless parameters that can be varied independently. This means it is sufficient to vary just α_{th}, α_{hy} and $(a-b)$, which corresponds to varying D_{th}, D_{hy} and z respectively. The parameters not being varied are fixed to the base parameters shown in Table 1. The results of this are shown in Figures 5, 6 and 7.

The numerical results agree well with the formula,

$$W_{rsf} \approx \frac{C(a-b)\rho c}{f_o \Lambda} \frac{(\sqrt{\alpha_{hy}} + \sqrt{\alpha_{th}})^2}{V(f_o + 2(a-b))} \qquad (31)$$

This equation is shown by the dashed black lines in Figures 5, 6 and 7 for $C = 6.9$. While we have only shown a narrow range of values for α_{th}, slightly larger than the range quoted in *Rice* [2006], further simulations show that equation (31) provides a good fit across nearly three orders of magnitude. In the limit $f_o \gg (a-b)$, which is valid for almost all values of f_o and $(a-b)$ found in laboratory experiments, we can neglect $(a-b)$ in the denominator of equation (31) and
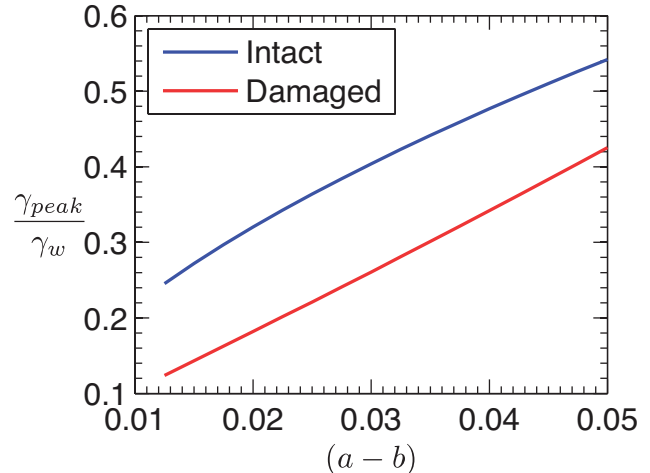
W_{rsf} becomes linear in $(a-b)$. The localized zone thickness is a balance between thermal pressurization, frictional rate-strengthening and hydrothermal diffusion, with hydrothermal diffusion entering through the lump diffusivity α of Rice [2006].

Using equation (31) we now make predictions for the localized zone thickness using the four parameter sets modeling a depth of 7 km. Using the superscript int to represent intact material, dam to represent damaged material, n for nominal parameter sets, and pa for path-averaged parameter sets, we find

$$W_{rsf}^{int,n} = 4\mu m \quad , \quad W_{rsf}^{int,pa} = 7\mu m \qquad (32a)$$

$$W_{rsf}^{dam,n} = 28\mu m \quad , \quad W_{rsf}^{dam,pa} = 44\mu m. \qquad (32b)$$

These predictions are close to the predicted values in *Rice et al.* [2013], and in good agreement with some field and laboratory observations, for example *De Paola et al.* [2008], *Brantut et al.* [2008], and *Kitajima et al.* [2010]. These observations are discussed in detail in the introduction to *Rice et al.* [2013]. Due to more efficient hydraulic diffusion and less efficient thermal pressurization, we predict a wider localized zone for the damaged parameter sets. Parameter variations due to changes in pore pressure and temperature, which are accounted for using the path-averaging method from *Rice* [2006], increase the localized zone thickness by $60 - 75\%$.

Next we evaluate (31) for the parameter sets modeling a depth of 1 km from Table 2, finding,

$$W_{rsf}^{1km,int} = 30\mu m \quad , \quad W_{rsf}^{1km,dam} = 216\mu m. \qquad (33)$$

Wider localized zones are predicted at shallower depths, as predicted in *Rice et al.* [2013]. Changes in gouge properties due to changes in pore fluid pressure and temperature were not accounted for when making these predictions. Tentatively assuming that the percentage increase in thickness is the same as the values for a depth of 7 km we predict a width of ~ 55 μm for an intact material and ~ 340 μm.

5.3. Impact of localization on shear strength evolution

During our calculations we also track the shear strength. Figure 8 shows the shear strength evolution when we use the path-averaged parameters for a damaged material, $h = 1$ mm and $V = 1$ m/s, the same calculation used to produce the localized straining profile in Figure 3. For comparison we also show the shear strength evolution when the gouge layer is forced to deform uniformly, with the uniform solution calculated by setting $\dot{\gamma} = \dot{\gamma}_o$ throughout the gouge layer and approximating the shear stress using the pore pressure in the center of the gouge layer,

$$\tau(t) = f_o[\sigma_n - p(0,t)]. \tag{34}$$

This calculation is very similar to those performed in *Rempel and Rice* [2006]. Henceforth, the solution where the gouge layer is forced to deform uniformly is referred to as the uniform shear solution, and the solution where the straining is allowed to localize within the gouge layer is referred to as the localized shear solution.

Initially the shear strength evolution is the same for the uniform shear solution and the localized shear solution. This corresponds to the early stages of deformation when straining has not had time to localize. As expected both the uniform shear and localized shear solutions also agree with the solution for uniform shear under undrained and adiabatic conditions from *Lachenbruch* [1980]. At the onset of localization we see a dramatic drop in strength, typically 20-40% of the initial strength $\tau_0 = f_o(\sigma_n - p_a)$. The exact strength drop at the onset of localization depends on the gouge layer width h, with more dramatic strength drops for larger values of h. These observation can be explained by recalling that thinner deforming zones lead to more rapid dynamic weakening. As the straining localizes the deforming zone thins leading to accelerated weakening. Larger values of h lead to larger strength drops at the onset of localization due to the larger contrast between the initial gouge layer width and final localized zone thickness. After straining has strongly localized the shear strength evolution is in excellent agreement with the Mase-Smith-Rice solution for slip on a plane.

Since the most rapid dynamic weakening is linked to strain rate localization, our results predict that the slip at which the most rapid dynamic weakening occurs is controlled by the gouge parameters. Motivated by this we now track γ_{peak} as a function of the gouge properties. Figures 9 and 10 shows the strain at which $\dot{\gamma}_{max}$ reaches its peak value divided by the weakening strain γ_w for thermal pressurization as a function of α_{hy}, and $(a - b)$. We see that smaller values of $(a - b)$, and thus larger values of z, lead to smaller value of γ_{peak}/γ_w. This means that not only does frictional rate-strengthening limit localization, it also slows the rate at which a localized zone develops. The dependence of γ_{peak} on α_{hy} is the reverse of that observed for $(a - b)$. Whenever the localized zone thickness is over an order of magnitude thinner than the gouge layer thickness, smaller values of α_{hy} lead to larger values of γ_{peak}/γ_w. The increase in γ_{peak} for larger values of α_{hy} occurs when the localized zone thickness becomes comparable to the gouge layer thickness. Since the thermal diffusivity is relatively well constrained we do not show the dependence of γ_{peak} on α_{th}, but the results are qualitatively very similar to those observed for α_{hy}.

It should be emphasized that this dependence of γ_{peak} on α_{hy} may not transfer to other geometries. In our system the localization is initiated by hydrothermal diffusion from the gouge layer into the half-spaces, leading to larger pore pressures and strain rates in the center of the gouge layer, and thus the formation of a localized zone. Lower values of the bulk hydrothermal diffusivity α defined in equation (13)

limit diffusion into the half-spaces leading to larger values of γ_{peak}. If localization is instead initiated by heterogeneities within the gouge layer then the dependence of γ_{peak} on α_{hy} could be very different. This link between localization and heterogeneities within the gouge layer is the subject of ongoing work.
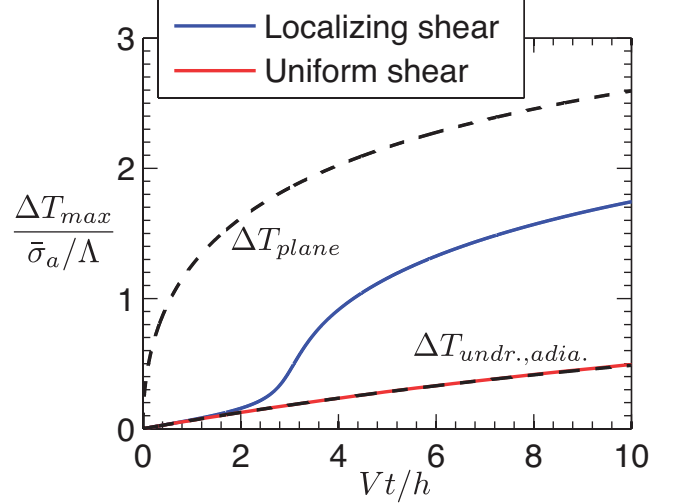

Figure 11. Rate-strengthening friction: A plot showing how the maximum temperature rise, $\Delta T_{max} = T_{max} - T_a$, in the gouge layer evolves for localized and uniform shear using the path-averaged parameters for a damaged material, $h = 1$ mm and $V = 1$ m/s. The initial behavior, before localization and diffusion become important, is well described by the undrained adiabatic solution of *Lachenbruch* [1980] (marked $\Delta T_{undr.,adia.}$). As straining localizes the frictional heating is focused into a zone much narrower than the gouge layer thickness, leading to a sharp temperature rise. After localization the localized shear solution mirrors the Mase-Smith-Rice slip on a plane solution (marked ΔT_{plane}), but the slip on a plane solution never provides a good approximation for maximum temperature rise.

If the gouge layer is sufficiently thick, or the slip is sufficiently small it may be possible that a fully developed localized zone will not occur during a seismic event. To estimate when this will happen we assume that for a wide gouge layer $\gamma_{peak}/\gamma_w = 1$, which lead to a critical slip that must be reached for localization to fully develop

$$D_{loc.} = \frac{\rho c h}{f_o \Lambda} \tag{35}$$

Using a typical slip of 1 meter and the range of γ_w implied by the parameters in Table 1 we predict the critical gouge layer thickness above which localization does not have sufficient time to fully develop to be $6.6 - 20$ cm. If the gouge layer thickness is only slightly less than the critical thickness then the majority of shear will have occurred with an underdeveloped localized zone, with full localization occurring just before deformation ceases.

A underdeveloped localized zone will have three important consequences. First, even though strain rate localization is occurring, there may be little evidence of highly localized shear in the final strain profile. Second, since the most rapid dynamic weakening occurs during the most rapid localization, we would expect a much smoother strength evolution profile than the one shown in Figure 8. Finally, since the straining is never focused into a narrow zone we would expect a significantly lower temperature rise.
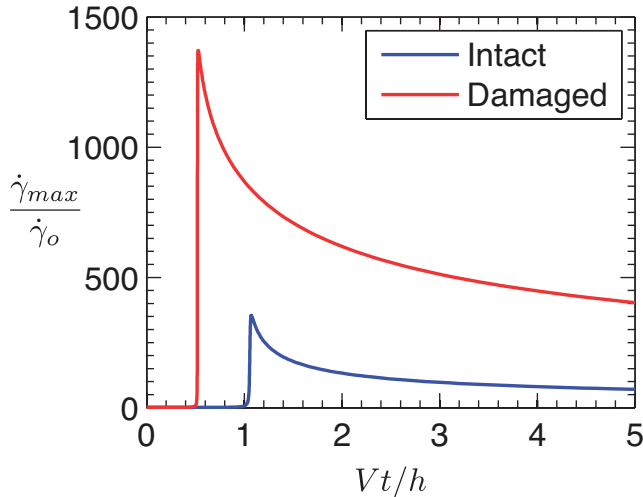
Figure 12. Gouge dilatancy: A plot showing how the maximum strain rate $\dot{\gamma}_{max}$ evolves for the path-averaged parameters modeling an intact and a damaged material, for $V = 1$ m/s and $h = 0.5$ mm. As predicted by the linear stability analysis there is an initial transient of intense strain rate localization followed by decay to homogeneous straining. In contrast with the frictional strengthening case, the damaged material shows more intense localization.

Figure 13. Gouge dilatancy: A plot showing how the peak strain rate $\dot{\gamma}_{peak}$ depends on the dimensionless parameter $E = \varepsilon/(\beta\bar{\sigma}_a)$ for the dilatancy only system using the path-averaged parameters modeling an intact and a damaged material, $V = 1$ m/s and $h = 0.5$ mm. For both parameter sets we observe larger peak strain rates for smaller values of E, corresponding to narrower localized shear zones. For all but the smallest values of E our results are well described by equation (47), and for each parameter set this formula is shown by the dashed black line.

5.4. Influence on maximum temperature rise

Rempel and Rice [2006] showed that the undrained and adiabatic solution of *Lachenbruch* [1980] and the Mase-Smith-Rice slip on a plane solution. equations (16) and (19) respectively, are the end-member solutions for the maximum temperature rise in the uniform shear solution. However, the maximum temperature rise for the uniform shear solution will approach the Mase-Smith-Rice slip on a plane solution only at very large slips that may be larger than typical seismic slips.

We now compare the maximum temperature rise

$$\Delta T_{max}(t) = \max_y [T(y,t)] - T_a, \qquad (36)$$

predicted by our new localized shear solution with these two end-members, as well as the uniform shear solution. This is done using the path-averaged parameters for a damaged material, gouge layer width $h = 1$mm, and slip rate of $V = 1$ m/s, the same parameter set used to generate Figures 2, 3 and 8. The blue curve in Figure 11 shows the maximum temperature for the localized shear solution as a function of time. The symmetry of the system means that this maximum temperature occurs in the middle of the gouge layer, which in our coordinate system is $y = 0$. Alongside this is plotted the maximum temperature rise for the uniform shear solution in red, as well as the two end-member solutions for undrained and adiabatic conditions, and the Mase-Smith-Rice slip on a plane solution. The onset of localization is accompanied by a large increase in the maximum temperature as frictional heating is focused into a narrow zone in the center of the gouge layer. After a slip of 10 mm the temperature rise for the localized shear solution is over three times larger than the temperature rise for the uniform shear solution. For the parameters used in this simulation this corresponds to a difference of $\sim 580°$C.

Initially the uniform shear solution and localized shear solution are in excellent agreement with equation (16), which describes the temperature evolution under undrained and
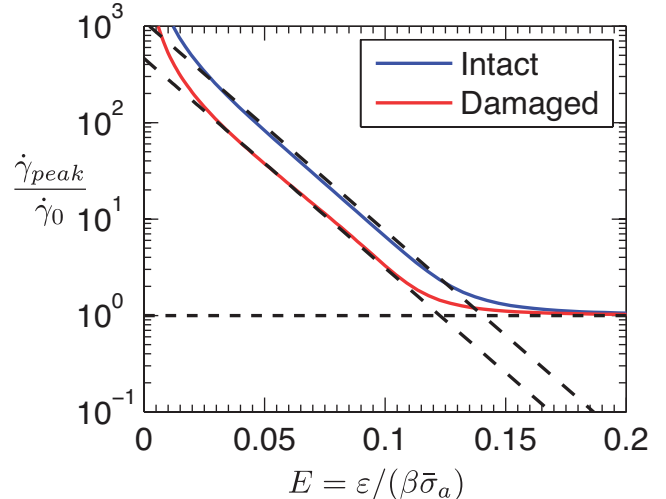
adiabatic conditions. After localization the solution mirrors the solution for slip on a plane, as would be expected when all of the deformation is accommodated in a very narrow zone, though the slip on a plane solution still does not give an accurate prediction of the maximum temperature since it neglects the initial stages of shear when deformation is distributed throughout the gouge layer. The maximum temperature rise for the localized shear solution will never approach the slip on a plane solution due to a pair of instabilities that cause the zone of localized straining to move across the gouge layer, thus distributing the frictional heating across a wider zone.

Finally we investigate how the magnitude of the temperature rise associated with localization depends on the gouge parameters. To quantify this we study the maximum heating rate,

$$\left(\frac{\partial T}{\partial t}\right)_{peak} = \max_{t,y}\left(\frac{\partial T}{\partial t}\right). \qquad (37)$$

This is found to be a decreasing function of α_{hy}, α_{th} and $(a - b)$. This is easily understood by noticing that the localized zone thickness W_{rsf} is an increasing function of α_{hy}, α_{th} and $(a-b)$. Parameters that predict a narrower localized zone will lead to a larger maximum heating rate as straining is focused more intensely.

6. Stabilization by Dilatancy Only

Having considered the case where the localized zone is stabilized by frictional strengthening alone, we now consider a system with constant (i.e. rate-independent) friction where stabilization is provided by dilatancy only. For this case the model simplifies to,

$$\frac{\partial T}{\partial t} = \frac{\tau\dot{\gamma}}{\rho c} + \alpha_{th}\frac{\partial^2 T}{\partial y^2}, \qquad (38a)$$

$$\frac{\partial p}{\partial t} = \Lambda\frac{\partial T}{\partial t} - \frac{\varepsilon}{\beta\dot{\gamma}}\frac{\partial\dot{\gamma}}{\partial t}. \qquad (38b)$$

Mechanical equilibrium combined with constant friction requires that p be a function of t alone, and the shear strength is given by $\tau = f_o[\sigma_n - p(t)]$.

6.1. Linear stability predictions

As with the frictional strengthening only case, *Rice et al.* [2013] analyzed small perturbations away from this uniform shear solution, finding the linearized equation for a strain rate perturbation $\dot{\gamma}_1$ with a wavelength λ,

$$\frac{d\dot{\gamma}_1}{dt'} = \left(\frac{1}{E} \exp\left(-t'\right) - \frac{1}{\hat{\lambda}^2} \right) \dot{\gamma}_1 + \frac{C}{\hat{\lambda}^2}, \qquad (39)$$

Here we have defined the dimensionless time $t' = (\dot{\gamma}_o/\gamma_w)t$, E is defined as in equation (10), $\hat{\lambda}$ is a dimensionless wavelength defined by,

$$\hat{\lambda} = \frac{\lambda}{L_{thd}} \quad , \quad L_{thd} = 2\pi\sqrt{\alpha_{th}t_w} \qquad (40)$$

and C is a constant set by the initial perturbations in strain rate and temperature,

$$C = \dot{\gamma}_1(0) - (\Lambda\beta\dot{\gamma}_o\varepsilon)T_1(0). \qquad (41)$$

Rice et al. [2013] showed that the large slip solution to (39) is $\dot{\gamma}_1 \to C$ as $t \to \infty$. However, for gouge layer thicknesses exceeding a critical width W_{dil} the strain rate perturbation will undergo transient growth. This transient growth is interpreted as strain rate localization. By determining the maximum values of $\dot{\gamma}_1$ it was shown that small values of E correspond to more extreme growth. This can be understood in the stabilization framework since small values of E correspond to small dilatant suctions, less stabilization, and thus more intense localization.

6.2. Localized zone thickness

The solution to the linearized equation (39) predicts very large strain rate perturbations, far beyond the magnitudes at which the linearization is valid, unless the initial strain rate perturbations are unrealistically small, on the order of 10^{-10} to 10^{-20} of $\dot{\gamma}_o$ or less (see *Rice et al.* [2013]). To account for nonlinear effects we now solve the full system numerically for a slip rate $V = 1$ m/s, and a gouge layer thickness $h = 0.5$mm. In all that follows the strain localization develops from an initial perturbation away from uniform straining,

$$\dot{\gamma} = \dot{\gamma}_o \left[1 + \delta \cos\left(\frac{2\pi y}{h} \right) \right], \qquad (42)$$

where $\delta = 10^{-3}$. Since $y = 0$ is located at the center of the gouge layer this initial perturbation is symmetric about the center of the gouge layer. The initial pore pressure and temperature are assumed to be the ambient values $p = p_a$ and $T = T_a$. Other values of δ were tested, as were initial conditions with a temperature perturbation, but the results are qualitatively the same. Slightly larger peak strain rates are observed for larger initial perturbations.

For strain rate localization stabilized by dilatancy alone we assume that the half-spaces adjacent to the gouge layer are thermally and hydraulically insulating. This is in contrast to the results for stabilization by frictional rate-strengthening alone presented in the previous section that accounted for transport of heat and pore fluid into the half-spaces. We assume the the half-spaces are thermally and hydraulically insulating to match the requirement that p is independent of y within the gouge layer. The symmetry of the no-flux boundary conditions at the edge of the gouge layer means that our simulations for a finite thickness gouge
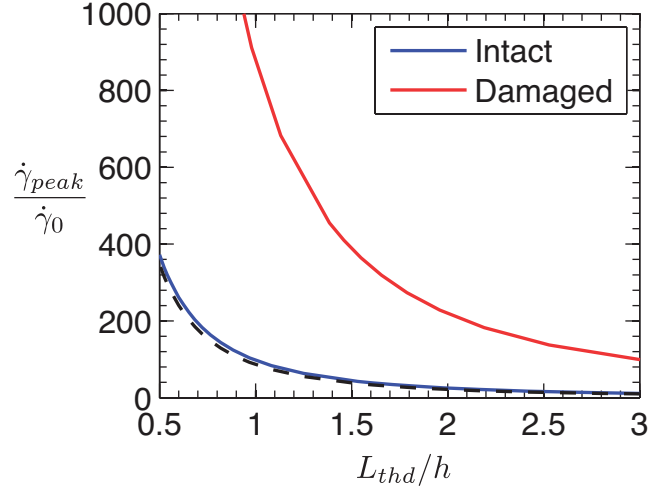

Figure 14. Gouge dilatancy: A plot showing how the peak strain rate $\dot{\gamma}_{peak}$ depends on the ratio of the thermal diffusion distance $L_{thd} = 2\pi\sqrt{\alpha_{th}t_w}$, where t_w is the characteristic weakening time for thermal pressurization, and the gouge layer thickness h. These simulations were produced using the path-averaged parameters modeling an intact and a damaged material, $V = 1$ m/s and $h = 0.5$ mm. Larger values of L_{thd}, corresponding to more efficient thermal diffusion, lead to lower peak strain rates and thus wider localized zones. The simulations are well fit by the formula given in equation (47), and this curve is shown by the dashed black line. No line is shown for the damaged parameters since the value of E is sufficiently small that equation (47) is no longer accurate.

layer are equivalent to the periodic domain considered in the companion paper *Rice et al.* [2013].

As before the maximum strain rate $\dot{\gamma}_{max}$ in the gouge layer is used as a proxy for localization, recalling that a higher maximum strain rate indicates more intense localization. The maximum strain rate is defined in equation (26). Figure 12 shows how $\dot{\gamma}_{max}$ evolves for the path-averaged parameters modeling intact and damaged material. As predicted by the linear stability analysis straining localizes within the gouge layer. Even when nonlinear effects are accounted for the strain rate localization is transient. As in the system where strain rate localization is stabilized by frictional rate-strengthening alone the maximum temperature within the gouge layer increases rapidly as straining localizes, and this is accompanied by a sudden reduction in the shear strength. The spatial distribution of straining is well described by a Gaussian function throughout the simulations.

We can understand the transient nature of localization by rewriting (38a) and (38b) as,

$$\frac{\varepsilon}{\beta\dot{\gamma}} \frac{\partial\dot{\gamma}}{\partial t} = \Lambda\left(\frac{\tau\dot{\gamma}}{\rho c} + \alpha_{th}\frac{\partial^2 T}{\partial y^2} \right) - \frac{\partial p}{\partial t} \qquad (43)$$

The high strain rates associated with localization lead to increased thermal pressurization and a sudden drop in strength, leading us to look at the large slip limit in which the pore pressure approaches the normal stress,

$$p \to \sigma_n \quad , \quad \frac{\partial p}{\partial t} \to 0. \qquad (44)$$

This leads to,

$$\frac{1}{\dot{\gamma}} \frac{\partial\dot{\gamma}}{\partial t} = \frac{\alpha_{th}\Lambda\beta}{\varepsilon} \frac{\partial^2 T}{\partial y^2}. \qquad (45)$$

The zero flux boundary conditions at the end of the gouge layer and the symmetry about the center of the gouge layer allow us to deduce that T has its maximum value at $y = 0$ and minimum values at $y = \pm h/2$ for the initial perturbation given in equation (42). Integrating equation (38b) we can also show that the maximum and minimum values of T coincide with the maximum and minimum values of $\dot{\gamma}$. Thus, using equation (45) we conclude that at large slips the maximum strain rate will decay and the minimum strain rate will grow. As the maximum and minimum values of $\dot{\gamma}$ approach each other the straining profile in the layer must return to uniform shear, meaning that strain rate localization will always be transient. If we had attempted to model transport of pore fluid and heat into the adjoining half-spaces it may have taken much longer for the limit described in equation (44) to be reached, possibly allowing straining to remain at peak localization for longer than is observed in Figure 12.

Next we quantify the intensity of localization by tracking the peak strain rate as a function of the two controlling dimensionless parameters

$$E = \frac{\varepsilon}{\beta \bar{\sigma}_a} \quad , \quad L_{thd} = 2\pi\sqrt{\alpha_{th} t_w}. \tag{46}$$

By considering the dimensionless parameters we can reduce the number of parameters we must vary dramatically. Note that when setting $\lambda = h$ the parameter $\hat{\lambda} = \lambda/(2\pi\sqrt{\alpha_{th} t_w})$ from *Rice et al.* [2013] becomes the ratio of the gouge layer thickness and the diffusional lengthscale L_{thd}. Having discussed how we can use the maximum strain rate as a proxy for intensity of localization, we next use the peak strain rate $\dot{\gamma}_{peak}$ defined in equation (30) to quantify the width of localized zone at peak localization. Since for stabilization by dilatancy alone our initial perturbation has a maximum value on $y = 0$ the peak strain rate $\dot{\gamma}_{peak}$ will always occur at $y = 0$. $\dot{\gamma}_{peak}$ can be thought of as the maximum value ever achieved by $\dot{\gamma}_{max}(t)$. Figures 13 and 14 show how $\dot{\gamma}_{peak}$ varies with the two dimensionless parameters E and L_{thd}. In agreement with the linear stability predictions, we observe that smaller values of E lead to larger values of $\dot{\gamma}_{peak}$ and thus more intense localization.

Except for the very lowest values of E, the simulations can be well fit using the equation,

$$\frac{\dot{\gamma}_{peak}}{\dot{\gamma}_o} = 30\pi^2 \frac{h^2}{L_{thd}^2} e^{-50E}, \tag{47}$$

as shown by the black dashed lines in Figures 13 and 14. As E gets very small the peak strain rate starts to increase more rapidly than predicted by equation (47), and as $E \to 0$ the peak strain rate must go to infinity. A fitting curve is not shown for the damaged parameters in Figure 14 since the value of E for this parameter set is in the range of values where (47) does not accurately describe our results. For this parameter set the peak strain rate is still proportional to $\hat{\lambda}^2$. In theory the exponential in equation (47) could be replaced by a more complicated function of E that diverges as $E \to 0$, though we did not attempt to do this due to the computational expense of simulations for very low values of E, and the fact that the localized zone thicknesses in this limit will approach the size of individual grains within the gouge. We emphasize that the exact numerical values in (47) depend on the size of the initial perturbations, though the qualitative picture is the same for a wide range of initial perturbations.

Equation (47) can be rearranged to give the peak strain rate in dimensional variables,

$$\dot{\gamma}_{peak} = \frac{15V^2}{2\alpha_{th}\gamma_w} \exp\left(-\frac{50\varepsilon}{\beta\bar{\sigma}_a}\right). \tag{48}$$
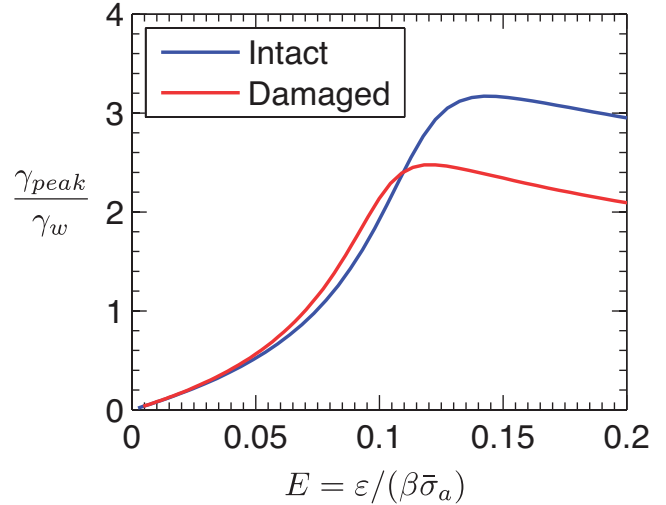

Figure 15. Gouge dilatancy: A plot showing how γ_{peak}, the strain at which peak localization occurs, depends on E. These simulations were done using the path-averaged parameters for an intact and damaged material, $V = 1$ m/s and $h = 0.5$ mm. Our results show that when E is small enough that transient strain rate localization occurs γ_{peak} is an increasing function of E, with small values of E leading to small values of γ_{peak}. This means that the most intense localized zones develop very rapidly. Very little difference is observed between the two parameter sets, which can be explained by noting that γ_{peak} is relatively insensitive to changes in L_{thd}, as shown in Figure 16.

As in the frictional strengthening only scenario, this formula is independent of the gouge layer width h, and the peak strain rate is controlled solely by the internal properties of the gouge material. We can relate this to a localized zone width W_{dil} using the relation

$$W_{dil} = \sqrt{\frac{2}{\pi}} \frac{V}{\dot{\gamma}_{peak}}, \tag{49}$$

which implies that,

$$W_{dil} = \sqrt{\frac{2}{\pi}} \frac{2\alpha_{th}\rho c}{15V f_o \Lambda} \exp\left(\frac{50\varepsilon}{\beta\bar{\sigma}_a}\right). \tag{50}$$

The localized zone thickness is set by a balance between thermal pressurization, thermal diffusion, and dilatant strengthening.

The formula in equation (50) is now used to predict the localized zone width for the different parameter sets. First for the four parameter sets modeling a depth of 7 km we find,

$$W_{int,n} = 1.32\mu m \quad , \quad W_{int,pa} = 1.21\mu m \tag{51a}$$
$$W_{dam,n} = 1.85\mu m \quad , \quad W_{dam,pa} = 1.08\mu m. \tag{51b}$$

All four parameter sets predict a localized zone between 1 μm and 2 μm wide. The range of values is much more compact than for the frictional rate-strengthening only analysis. Damaged and intact parameters predict comparable thicknesses.

Next we look at the parameters modeling a depth of 1 km, predicting the localized zone thicknesses,

$$W_{1km,int} = 52\mu m \quad , \quad W_{1km,dam} = 14\mu m. \tag{52}$$

The predicted localized zone thicknesses are an order of magnitude larger than our predictions for a depth of 7 km, but still on the micron-scale. This is largely due to the sensitive dependence of W_{dil} on the ambient effective stress $\bar{\sigma}_a$.

The damaged parameters predict a thinner zone than the intact material, the exact opposite of the dependence predicted in the strengthening-only system. These predictions for W_{dil} must be used with caution due to the sensitive dependence on ε. We have used a parameter extracted from a single set of low strain rate experiments, but ε may be different at higher strain rates. An order of magnitude increase in ε leads to localized zone predictions on the tens of centimeters wide.

The formula for W_{dil} given in equation (50) is very different than the linear stability prediction from *Rice et al.* [2013] for the critical gouge layer thickness above which transient strain rate localization is expected. This means that the linear stability analysis cannot be used to make quantitative predictions for the localized zone thickness when localization is stabilized by dilatancy alone.

Since the shear strength evolution is linked to the onset of localization we also track the strain γ_{peak} at which the peak strain rate is achieved, where the peak strain rate is defined in equation (30). Figures 15 and 16 show γ_{peak}/γ_w as a function of E and L_{thd}. The critical strain γ_{peak} increases with ε but is relatively insensitive to changes in L_{thd} provided that straining localizes to a zone much thinner than the gouge layer thickness. Comparing this dependence on ε with the results from the previous section we see that, for both frictional rate-strengthening and dilatancy, a thicker localized zone corresponds to a larger value of γ_{peak}; a weaker localization limiting mechanism not only allows a narrower localized zone to form, it also allows this zone to develop faster.

6.3. Strain vs. strain rate localization

It is virtually impossible to observe in-situ strain rate profiles from seismic events or high-velocity friction experi-
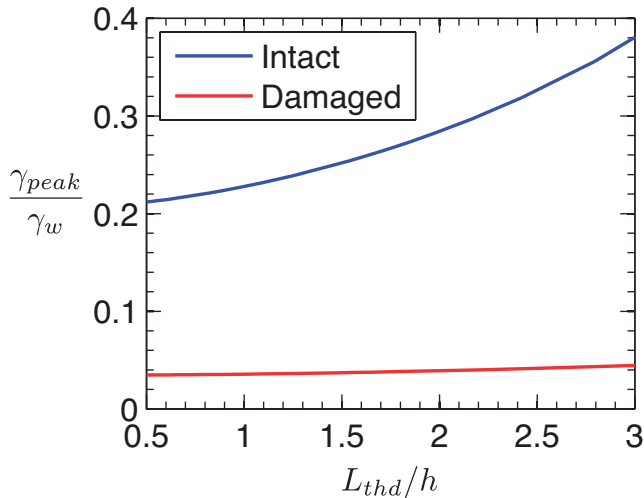

Figure 16. Gouge dilatancy: A plot showing how γ_{peak}, the strain at which peak localization occurs, depends on the ratio of the thermal diffusion distance $L_{thd} = 2\pi\sqrt{\alpha_{th}t_w}$, where t_w is the characteristic weakening time for thermal pressurization, and the gouge layer thickness h. These simulations were done using the path-averaged parameters for an intact and damaged material, $V = 1$ m/s and $h = 0.5$ mm. Our results show that γ_{peak} is an increasing function of L_{thd}, though when the localized zone width is much smaller than the gouge layer thickness γ_{peak}/γ_w does not depend strongly on L_{thd}.

ments, with at best only the final strain pattern being observable. We now study the final strain profiles by integrating $\dot{\gamma}(y, t)$ to find the total strain $\gamma(y)$. Due to the transient nature of the localization for the dilatancy only system the final strain profile will be controlled by the amount of time spent straining in a localized fashion versus the amount of time spent straining in a more uniform state.

Figure 17 shows the final strain profile for three total slips of 1 cm, 10 cm, and 100 cm. These results were produced using the path-averaged parameters for a damaged material, $V = 1$ m/s and $h = 0.5$ mm. We observe a reduction in strain localization with increasing slip. This is because, for $Vt \gg h$, the transient strain rate localization lasts for a small fraction of the event and the gouge spends the majority of the simulation shearing uniformly. This leads to final strain profiles with very little strain localization. Thus, even when uniform straining is initially unstable, localization may not be observed in final strain profiles if a large quantity of deformation occurring at the end of the event is approximately uniform.

7. Inertial effects in the gouge layer

7.1. Model including inertia

In this section we study inertial effects within the gouge layer. *Rice* [2006] argued that inertial effects across the gouge layer are negligible due to the short distances over which hydraulic and thermal diffusion act. Following this we assumed that deformation within the gouge layer could be regarded as quasi-static, an assumption we now test in this section.

The inertial effects considered here are different from the inertial effects in the bulk material on either side of a fault associated with dynamic rupture. Since we consider kinematically applied slip, in which the motion of the two half-spaces is fixed to a uniform slip rate at $\pm V/2$, we have implicitly neglected unloading waves that would propagate into an elastic solid adjacent to the gouge layer.

Accounting for inertial effects within the gouge layer the equation for conservation of linear momentum becomes,

$$\rho\frac{\partial u}{\partial t} = \frac{\partial \tau}{\partial y}, \qquad (53)$$

where ρ is the density of the gouge material, and u is the local slip rate. This replaces equation (1), which modeled quasi-static deformation within the gouge layer. Differentiating equation (53) with respect to y we can express this in terms of the strain rate $\dot{\gamma}$,

$$\rho\frac{\partial \dot{\gamma}}{\partial t} = \frac{\partial^2 \tau}{\partial y^2}, \qquad (54)$$

recalling that the strain rate is defined as,

$$\dot{\gamma} = \frac{\partial u}{\partial y}. \qquad (55)$$

Using the same scalings as before, given in equation (8), the nondimensional form of equation (54) is,

$$I^2\frac{\partial \dot{\gamma}'}{\partial t'} = \frac{\partial^2 \tau'}{\partial y'^2} \quad , \quad I = \sqrt{\frac{\rho V^2}{(\sigma_n - p_a)}}, \qquad (56)$$

where primes indicate dimensionless variables. The dimensionless parameter I quantifies the effect of inertia in the gouge material. Interestingly the definition of I does not depend on the thickness of the gouge layer or the two diffusivities, and is a balance between an inertial stress and the
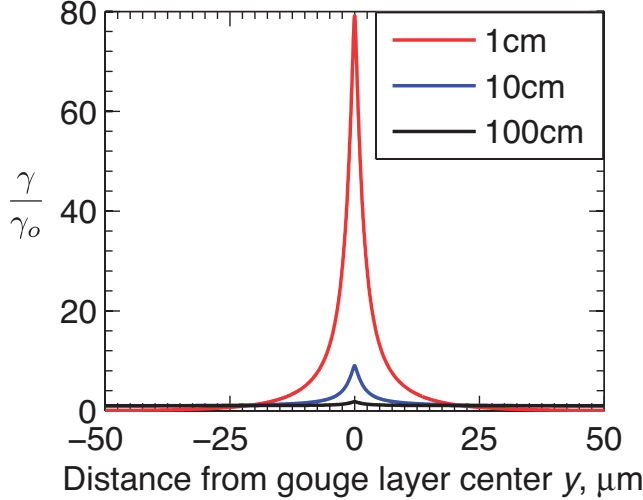
Figure 17. Gouge dilatancy: A plot of the final strain normalized by the average strain in the layer γ_o, for slips of 1 cm, 10 cm and 100 cm. These results were generated using the path-averaged parameters for a damaged material, $V = 1$ m/s, and $h = 0.5$ mm. We observe a decrease in strain localization with increasing slip. This can be understood by considering the transient nature of the localization; longer events will spend more time straining uniformly, and thus the effects of the transient strain rate localization will be less pronounced in the final strain profile.

ambient compressive effective stress. For the parameters in Table 1 and the slip rate $V = 1$ m/s we find $I = 0.0047$.

This inertial formulation of the problem is compatible with the kinematically applied slip condition (25), and thus the gouge material accommodates the correct amount of straining. To show this we integrate equation (54) with respect to y to find,

$$\frac{\partial}{\partial t}\left(\int_{-h/2}^{h/2} \dot\gamma \, \mathrm{d}y\right) = \left[\frac{\partial \tau}{\partial y}\right]_{-h/2}^{h/2}. \quad (57)$$

If the half-spaces adjacent to the gouge layer are in uniform motion, and thus have no change in strain, then the right hand side of this equation will vanish and the total strain rate accommodated by the gouge layer will not change with time. Assuming that the initial state of shearing is uniform, $\dot\gamma = \dot\gamma_o$ for $|y| < h/2$, we recover condition (25),

$$\int_{-h/2}^{h/2} \dot\gamma \, \mathrm{d}y = V. \quad (58)$$

This means that the results from the model accounting for inertial effects can be directly compared with the results that assumed mechanical equilibrium, allowing us to quantify the effects of inertia. For small values of I we expect inertial effects to be negligible and the two models to agree very well.

We now solve the frictional rate-strengthening only system for a range of values of I and compare with the results generated by the model that assumed mechanical equilibrium. As in previous sections we use the maximum strain rate $\dot\gamma_{max}$ in the layer as a function of time as a proxy for localization, with larger values of $\dot\gamma_{max}$ indicating a thinner deforming zone. Figure 18 shows $\dot\gamma_{max}$ as a function of time for the nominal parameters describing a damaged material, a gouge layer width $h = 0.5$ mm, $V = 1$ m/s, and

$I = 10^{-1.5}$, $I = 10^{-1}$, and $I = 10^{-0.5}$. For $I = 10^{-1.5}$ the inertial and mechanical equilibrium models agree very well, but for $I = 10^{-1}$ and $I = 10^{-0.5}$ the inertial results begin to differ from the mechanical equilibrium solutions. More noticeable differences are observed for the largest value of I.

To quantify these inertial effects we now track the peak strain rate $\dot\gamma_{peak}$ and the time t_{peak} at which this peak strain rate occurs as a function of I. This is shown in Figure 19 for the nominal parameters modeling intact and damaged material, $h = 0.5$ mm, and $V = 1$ m/s. To allow easy comparison between the two parameter sets the results are normalized by the value from the mechanical equilibrium model; a value of unity means that the results from the mechanical equilibrium and inertial models agree exactly. As seen in the simulations shown in Figure 18, for very small values of I the two models agree almost exactly, but as I increases inertia becomes important and the two models diverge. Inertial effects within the gouge layer lead to lower values of $\dot\gamma_{peak}$ and larger values of t_{peak}, indicating that inertial effects lead to wider localized zones that take longer to develop.

Using the results shown in Figures 18 and 19 we choose a value of $I = 0.1$ as a cutoff above which inertial effects become important. An argument could be made for a slightly larger or smaller critical value of I but this appears to be the correct order of magnitude. This critical value allows us to define a critical slip rate,

$$V_c = \sqrt{\frac{\bar{\sigma}_a}{100\rho}}. \quad (59)$$

Inertial effects will become important when slip rates exceed this critical value, and will act to limit localization.

Here we chose the $I = 0.1$ as an estimate of the critical value based on simulations performed using two different parameter sets. A fuller analysis would find the critical value of I for a much wider range of parameters, showing how it varies as the intensity of strain rate localization varies.
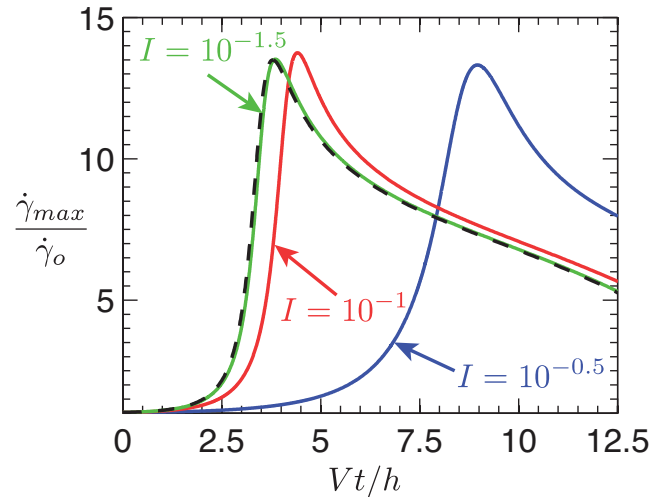

Figure 18. Rate-strengthening friction: A plot showing how maximum strain rate evolves in the inertial model for $I = 10^{-0.5}, 10^{-1}$ and $10^{-1.5}$. This plot was created using the nominal parameters modeling a damaged material, $h = 0.5$ mm and $V = 1$ m/s. For comparison the solution when mechanical equilibrium is assumed is shown by the dashed black line. For the lowest value of I the inertial and equilibrium solutions agree almost exactly, while for the larger values we see deviation away from the equilibrium solution.

7.2. Implications for high-velocity friction experiments

We now use the critical slip rate V_c to comment on the role of inertia during high-velocity friction experiments. These experiments are typically performed using a rotary shear configuration and allow experiments to be performed at seismic slip rates, albeit at compressive stresses much lower than those present during seismic events [*Brantut et al.*, 2008; *Kitajima et al.*, 2010; *Reches et al.*, 2012; *Smith et al.*, 2013]. Highly localized shear zones are commonly observed in high-velocity friction experiments. A fuller discussion of these observations can be found in the introduction to *Rice et al.* [2013].

To estimate V_c for conditions typical in high-velocity friction experiments we use $\sigma_n = 0.6$ MPa and assume that the initial pore pressure is negligible compared with this normal stress. The gouge density appropriate for laboratory conditions is assumed to be the same as that given in Tables 1 and 2. Combining these values leads to a critical slip rate of $V_c = 1.46$ m/s. This value of V_c is higher than the 1 m/s slip rates normally used in high-velocity shear experiments, and thus we conclude that inertial effects within the gouge layer are not playing a significant role in limiting localization in high-velocity friction experiments.

Additional simulations in which the half-spaces are undrained and adiabatic show that when pore pressures have risen to a significant fraction of the normal stress the appropriate definition of I may be based on the current effective stress not the ambient effective stress. Motivated by this we make an estimate for V_c based on a much lower effective stress $\bar{\sigma}_a = 0.15$ MPa, which is intended to model a gouge with a compressive stress $\sigma_n = 0.6$ MPa and a pore pressure that has risen to seventy-five percent of the normal stress. In this case we find $V_c = 0.73$ m/s. Thus, for this scenario we would predict that inertial effects within the gouge are not negligible when the applied slip rate is 1 m/s. However, since the critical slip rate V_c is only exceeded by a small amount the actual limiting of localization by inertia would probably not be dramatic. Figure 19 shows that significant localization limiting only occurs once $I > 0.3$.

7.3. Implications for natural faults

Next we discuss the importance of inertial effects during earthquakes. Consider a fault at a depth D where the depth is measured in kilometers. The effective overburden stress is $(\rho - \rho_w)gD$, assuming hydrostatic fluid pressure. Typically $\rho = 2.8\rho_w$ so the gradient in overburden effective stress is 18 MPa/km and $\bar{\sigma} = 18D$ MPa. This is consistent with the values of $\bar{\sigma}_a$ we chose in the parameter sets given in Tables 1 and 2. For a depth of 1 km we set $\bar{\sigma}_a = 18$ MPa, and for a depth of 7 km we set $\bar{\sigma}_a = 126$ MPa.

Taking the values in Table 1 we can calculate a critical slip rate $V_c = 21.2$ m/s for a depth of 7 km. Since the hydraulic parameters do not enter the formula for V_c this value is the same for all four parameter sets. This is compared with a typical coseismic slip rates of 1 m/s, justified as an average earthquake slip rate in *Rice et al.* [2013]. Since V_c is much larger than typical coseismic slip rates we conclude that, as predicted in *Rice* [2006], inertial effects within the gouge layer are negligible at seismic depths. Using our formula for V_c we can calculate what depth D must be exceeded for inertial effects to be negligible. Setting $V_c = 1$ m/s we find that this critical depth is just 15 meters, and thus inertial effects will be negligible throughout the seismogenic zone.

So far the analysis in this section has compared V_c to a typical coseismic slip rate of 1 m/s. However, near the tip of a dynamically propagating fracture the slip rates will be significantly larger. The peak slip velocity $V = 300$ m/s from *Noda et al.* [2009], which is taken as a typical peak slip rate during dynamic rupture, is far in excess of our prediction for V_c. This may mean that shear localization is initially limited by inertial effects even though they are unimportant throughout the vast majority of the rupture. Using our formula for $\bar{\sigma}_a$ as a function of depth we find that this picture, in which inertial effects are important near the crack tip yet unimportant for the majority of a rupture, is valid for all depths spanning the seismogenic zone.

Interestingly *Noda et al.* [2009] noted that the slip rates above ~ 100 m/s persist for only 1 μs, which corresponds to a slip of just 100 μm. Comparing this small slip with the results in Section 5, which showed that a finite strain is required for the localized zone to develop, we conclude that near the tip localization may not have time to fully develop.

A better description of localization near the tip of a dynamically propagating fracture that balances the high slip rates, small slips and inertial effects is still required. It may be possible to use an analysis near the crack tip to predict a thickness of the deforming zone when inertial effects become unimportant and shear of the gouge material is well described by the model in Section 2. This could then be used as an input for the model in Section 2, and the gouge layer thickness h would be reinterpreted as the thickness of the deforming zone when inertial effects become unimportant. Of course there may be some scenarios in which negligible localization occurs near the tip and the initial width of the deforming zone will be equal to the gouge layer thickness.

As mentioned in the previous subsection, when pore pressures have risen to a significant fraction of the normal stress the appropriate definition of I may be based on the current effective stress not the ambient effective stress. We highlight two scenarios when this distinction may be important.

Simulations that account for thermal decomposition show that the onset of the reaction is accompanied by a large pore pressure increase that can drive the gouge layer into a regime where the pore pressure exceeds the normal stress [*Sulem and Famin*, 2009]. As the pore pressure approaches the normal stress inertial effects will become important within the gouge layer and will act to widen the deforming zone. Since this widening will spread frictional heating over a wider zone, which will lead to slower pore pressure rises at the location of peak pore pressure, delocalization driven by inertial effects may be one mechanism to stop the maximum pore pressure exceeding the normal stress.

The other scenario in which inertial effects may become important as pore pressures approach the normal stress is near the trailing edge of a dynamically propagating rupture. We can estimate the minimum effective stress $\bar{\sigma}_{min}(t)$ in the late stages of rupture using the Mase-Smith-Rice slip on a plane solution. Using the asymptotic expansion for the complementary error function valid at large slips this leads to,

$$\frac{\bar{\sigma}_{min}}{\bar{\sigma}_a} = \sqrt{\frac{L^*}{\pi\delta}}, \qquad (60)$$

where $\delta = Vt$ is the total slip accommodated across the gouge layer. Defining $I_{cur.}$ in a similar fashion to the definition of I but using the current minimum effective stress $\bar{\sigma}_{min}$ we find,

$$I_{cur.} = \left(\frac{\pi\delta}{L^*}\right)^{1/4} I. \qquad (61)$$

The four parameter sets in Table 1 predict values of L^* between 1.69 mm and 57.7 mm. Using a typical seismic slip of one meter this predicts values of $I_{cur.}$ between a factor of 2.71 and a factor of 6.57 larger than I. For a larger slip of ten meters this range of values increases to 4.83 and 11.68. These values of $I_{cur.}/I$ mean that inertial effects may become important near the trailing edge of a rupture for small values of $\bar{\sigma}_a$, which correspond to shallow events, and small values of L^*. However, the range of values for L^* means that this behavior should not be expected for all earthquakes. Since inertial effects act to limit localization, and having

shown the link between localization and dynamic weakening, we hypothesize that the gradual onset of inertial effects at the trailing edge of a rupture may lead to a slowdown in dynamic weakening. Without further work it is hard to quantify how much strengthening this mechanism could lead to at the trailing edge, and if this would be a viable mechanism to promote ruptures that propagate as self-healing pulses (as opposed to crack-like ruptures).

7.4. Links with granular flow

Discrete simulations of granular flows commonly quantify the effects of particle inertia using a dimensionless parameter known as the inertia number [*Da Cruz et al.*, 2005; *Forterre and Pouliquen*, 2008], which is defined as

$$I_{gran.} = \dot{\gamma} d \sqrt{\frac{\rho_g}{P}}. \tag{62}$$

Here ρ_g is the density of the grains, P is the applied pressure, $\dot{\gamma}$ is the applied shear rate, and d is the grain size. Assuming that the density of the grains is equal to the density of the porous material per unit reference volume, an assumption that is justified for a gouge material with a low porosity, and that the pressure is equivalent to the ambient compressive stress $\bar{\sigma}_a$ we can write our dimensionless parameter I as

$$I = \frac{d}{h} I_{gran.}. \tag{63}$$

Our parameter I is equal to the inertia number multiplied by the ratio of the grain diameter and the gouge layer thickness. When shear is highly localized it may be more appropriate to use the current width of the deforming zone, W_{rsf} when localization is stabilized by frictional rate-strengthening alone, instead of the initial gouge layer thickness h. This corresponds to setting $\dot{\gamma} = V/W_{rsf}$ instead of $\dot{\gamma} = V/h$ in the definition of $I_{gran.}$. For either choice we expect $I_{gran.}$ to be at least an order of magnitude greater than I.

We now compare the point at which inertial effects across the gouge layer, as described by equation (54), become important with the point at which the inertia of individual grains becomes important. *Da Cruz et al.* [2005] cites the critical value $I_{gran.} = 0.1$ as the point at which the inertia of individual grains becomes important. Our simulations show that inertial effects across the gouge layer become important when $I > 0.1$. Since $I_{gran.}$ is at least an order of magnitude larger than I we deduce that the inertia of individual particles should become important before the inertial effects across the gouge layer become important. However, without determining how the critical value of I inferred from Figure (19) varies with the gouge properties we cannot be sure that this conclusion is valid for all parameter choices.

There are some drawbacks with the granular simulations used to find the critical value of $I_{gran.}$. First the granular simulations typically use particles that are roughly equal in size. This in stark contrast with the particle size distribution for the Punchbowl fault found in *Chester et al.* [2005], which showed that in a thin section the particle density was proportional to d^{-2}, where d is the grain size, for a d between 30 nm and 70 μm. This may mean that in a three-dimensional packing the particle density is proportional to d^{-3}. Another problem is the shape of the particles. Granular simulations frequently use discs in two-dimensional simulations, and sometimes spherical particles, while real fault gouge can have a much more diverse set of particles shapes. It is unclear if these considerations will dramatically alter the critical value of $I_{gran.} = 0.1$ at which the inertia of individual particles becomes important.

Our predictions for the localized zone thickness are not valid when the inertia of individual grains becomes important, though several options exist to create a new prediction. The first option is to linearize the friction laws in *Da Cruz*

et al. [2005] that account for the inertia of individual grains to find effective values of f_o and $(a - b)$, as suggested in equation (5) of *Rice et al.* [2013]. These effective values can then be used in the formulae for the localized zone thickness provided in this paper. Another option is to use a higher order continua or gradient theory that models the inertia of individual grains, and examples of how these models interact with thermal and pore fluid effects can be found in *Vardoulakis* [2002] and *Sulem et al.* [2011].

8. Discussion

8.1. Frictional rate-strengthening only

Our simulations predict micron-scale strain rate localization in a fluid-saturated gouge material. The strain rate profile has a Gaussian shape throughout the simulation, the same form assumed in previous models for thermal pressurization [*Andrews*, 2002; *Rempel and Rice*, 2006; *Noda et al.*, 2009; *Garagash*, 2012]. The excellent fit between the Gaussian function and our numerical simulations allows us to infer a width for the localized straining zone, which is taken to be twice the root mean square width of the Gaussian. Tracking this width as a function of the gouge layer thickness h we find that straining localizes to a zone that has a very weak dependence on the gouge layer thickness h. This means that the thickness of the localized zone is controlled by the gouge properties not the initial width of the gouge layer.

The nondimensionalization in subsection 2.5 shows that for localization stabilized by frictional rate-strengthening alone there are only three dimensionless parameters. One parameter quantifies the rate-strengthening component of the friction law and the other two compare the diffusion distances for thermal and hydraulic diffusion on timescales comparable to the characteristic weakening timescale for thermal pressurization with the gouge layer thickness. A parameter sweep over these three parameters allows us to determine the localized zone thickness at peak localization as a function of the gouge properties. The results are shown in Figures 5, 6 and 7, and our simulations are well fit by

$$W_{rsf} \approx \frac{6.9(a-b)\gamma_w}{f_o + 2(a-b)} \frac{(\sqrt{\alpha_{hy}} + \sqrt{\alpha_{th}})^2}{V} \tag{64}$$

The localized zone thickness is set by a balance between frictional rate-strengthening, thermal pressurization and hydrothermal diffusion. Comparing this formula with the linear stability prediction from *Rice et al.* [2013] we see one crucial difference. In the linear stability prediction hydrothermal diffusion enters through the sum of the diffusivities $\alpha_{hy} + \alpha_{th}$, while the results of our simulations are better fit by the *Rice* [2006] lump hydrothermal diffusivity $\alpha = (\sqrt{\alpha_{hy}} + \sqrt{\alpha_{th}})^2$ from the Mase-Smith-Rice slip on a plane solution. Since nonlinear terms are properly accounted for and the localized zone thickness is tracked from the initial instability all the way to peak localization, we consider the formula in this paper to be a better predictor for localized zone thickness than the formula given in *Rice et al.* [2013], which was based on a linear stability analysis. However, the two formulae produce very similar predictions, and in the limit where one diffusivity is much greater than the other the two formulae differ only in the constant fore-factor (π^2 in the linear stability analysis and 6.9 in the nonlinear simulations).

Using the parameters from *Rempel and Rice* [2006] modeling a depth of 7 km and frictional data from *Blanpied et al.* [1998] our formula for W_{rsf} predicts localized zone thicknesses between 4 μm and 44 μm. We also developed a set of hydraulic parameters intended to model a depth of 1 km,
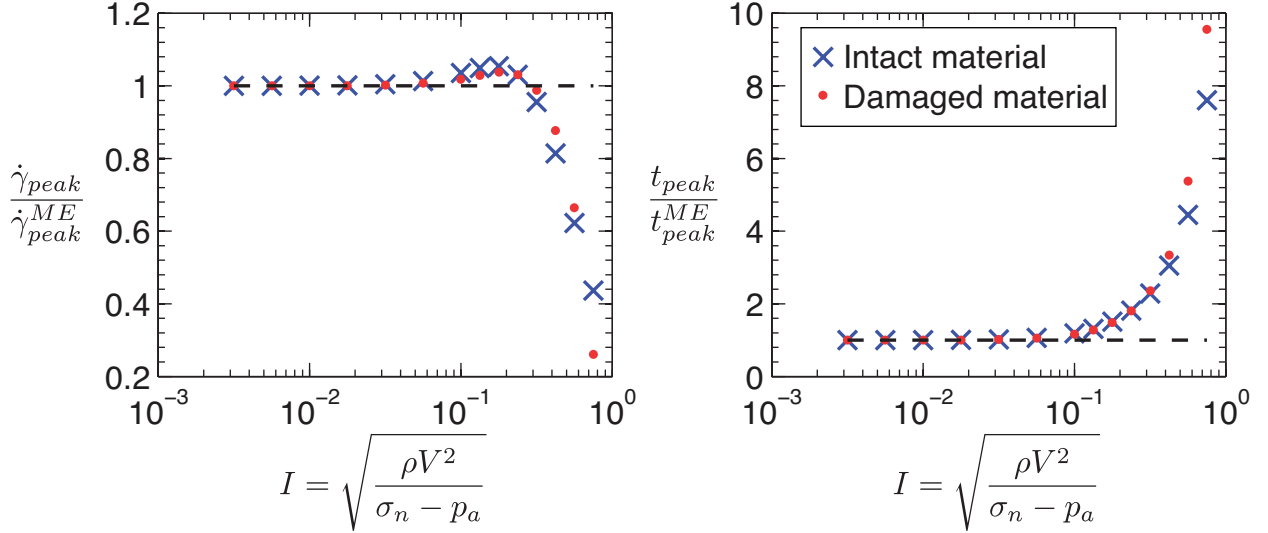
Figure 19. Rate-strengthening friction: A plot showing how the peak strain rate $\dot{\gamma}_{peak}$ and time t_{peak} at which this peak strain occurs vary with I for the nominal parameters modeling intact and damaged material, a gouge layer thickness $h = 0.5$ mm, and a slip rate $V = 1$ m/s. To allow easy comparison between the two parameter sets all values of $\dot{\gamma}_{peak}$ and t_{peak} are normalized by the values found when mechanical equilibrium is assumed. These mechanical equilibrium values are indicated by a superscript ME. Above $I = 10^{-1}$ inertial effects become important and the two models diverge. Inertial effects lead to two key differences. The value of $\dot{\gamma}_{peak}$ is decreased, which corresponds to a wider localized zone; the time t_{peak} at which peak localization occurs is larger indicating that the localized zone takes longer to develop.

a typical intersection depth for boreholes drilled into active faults. At shallower depths thermal pressurization is less efficient and hydraulic diffusion is more efficient, leading us to predict wider localized zones. For an intact material we predict a localized zone thickness of 31 μm, and for a damaged material, where damage is modeled as in *Rice* [2006], we predict a thickness of 217 μm. These values are very similar to those predicted in *Rice et al.* [2013]. A comparison between our predictions and observations from laboratory and field studies, and a discussion of other factors that that could alter our predictions, can be found in *Rice et al.* [2013].

The discussion above assumes that peak localization is achieved during a seismic event. However, this may not always be the case. Figures 9 and 10 show γ_{peak}, the nominal strain at which peak localization occurs, as a function of the gouge properties. A typical value for γ_{peak}/γ_w is 0.5. If the nominal strain is less than γ_{peak}, as will be the case for small slips or wide gouge layers, then the localized zone will not have time to fully develop. This will mean that final strain profiles will be thicker than the predictions from our formula for W_{rsf}.

8.2. Dilatancy only

For localization limited by dilatancy alone we see rapid strain rate localization, followed by a decay back to uniform shear. As for strain rate localization stabilized by frictional rate-strengthening alone, the localized zone has a Gaussian shape throughout the simulation. The system is controlled by just two dimensionless parameters, one modeling the strength of dilatancy and the other modeling the strength of thermal diffusion. Varying these parameters independently we find a formula for the localized zone thickness W_{dil} at peak localization

$$W_{dil} = \sqrt{\frac{2}{\pi}} \frac{2\alpha_{th}\rho c}{15 V f_o \Lambda} \exp\left(\frac{50\varepsilon}{\beta\bar{\sigma}_a}\right). \qquad (65)$$

As before the width of the localized zone is independent of the gouge layer thickness, and W_{dil} is set by the gouge properties. Using this formula and the parameters model-

ing a depth of 7 km (see Table 1) we predict localized zone thicknesses between ~ 1 and 2 μm. This range of values is lower than those predicted for frictional rate-strengthening alone, suggesting that dilatancy is less effective at limiting strain rate localization (if a wider localized zone is equivalent to more effective localization limiting). Our predictions fall into a more compact interval than our predictions for W_{rsf}. This is because the localized zone thickness is less sensitive to changes in hydraulic parameters than the frictional rate-strengthening system, and the hydraulic parameters are among the least constrained parameters in the system. We also predicted localized zone thicknesses at a depth of 1 km, with this depth intended to model a typical intersection depth for boreholes drilled in active faults. We predict $W_{dil} = 54$ μm for an intact material, and $W_{dil} = 15$ μm for a damaged material. Damaged parameters lead to thinner localized zones due to the increase in the storage capacity β. A larger storage capacity leads to less efficient limiting of localization by dilatant suctions. This is in contrast to the frictional rate-strengthening results that predicted wider localized zones for the damaged parameters.

The linear stability analysis in *Rice et al.* [2013] predicts transient growth followed by decay back to uniform shearing. However, the transient growth quickly leads to strain rate perturbations that violate the linearization assumptions. Our simulations properly account for nonlinear terms and qualitatively reproduce the transient growth predicted by the linear stability analysis. However, the quantitative predictions from the linear stability analysis do not agree with the widths inferred from our numerical simulations, and the formulae for W_{dil} predicted by the two methods have a very different structure. The linear stability predictions from *Rice et al.* [2013] provide a poor prediction of the localized zone thickness because the linearized model is applied beyond the point at which the linearization becomes invalid.

Finally we studied how the transient strain rate localization is expressed in final strain profiles. Figure 17 shows

the final strain profile for three different slips for the path-averaged parameters modeling a damaged material, $V = 1$ m/s and $h = 0.5$ mm. For slips that are large compared to the gouge layer thickness the majority of time will be spent shearing the gouge uniformly, leading to final strain profiles with little noticeable strain localization. As with the previous discussion of a localized shear zone that does not fully develop, this is another example of how final strain profiles can look like shearing was uniform even when uniform shearing is unstable. This difference between strain localization and strain rate localization must be considered when interpreting final strain profiles.

8.3. Localization and dynamic weakening

Rempel and Rice [2006] studied the shear strength evolution for a uniformly sheared gouge layer undergoing thermal pressurization. They verified that the initial stages of deformation are well described by the solution of *Lachenbruch* [1980] for uniform shear under undrained and adiabatic conditions, and the later stages of deformation are described by the Mase-Smith-Rice slip on a plane solution. Using this framework we studied the impact of strain rate localization on shear strength evolution.

Figure 8 shows that, for localization stabilized by frictional rate-strengthening alone, the onset of strain rate localization is accompanied by an acceleration in dynamic weakening, with the most rapid dynamic weakening coinciding with the most rapid thinning of the localized zone. As straining localizes the frictional heating is focused into a narrow zone leading to more efficient thermal pressurization. The early stages of deformation are still in good agreement with the uniform shear solution from *Lachenbruch* [1980]. During this period straining is localizing but is far from peak localization. After peak localization the shear strength is well described by the Mase-Smith-Rice slip on a plane solution. Our solutions are all for a fixed slip rate V. The results for strain rate localization stabilized by dilatancy alone also show this link between the onset of localization and accelerated dynamic weakening.

We found that the most rapid weakening corresponds to the time when the localized zone is thinning most rapidly. This means that the strain until peak localization, γ_{peak}, controls the slip at which the most rapid weakening occurs. For strain rate localization stabilized by frictional rate-strengthening alone γ_{peak} is an increasing function of $(a - b)$ and a decreasing function of α_{hy} and α_{th}. Values of γ_{peak}/γ_w are typically around 0.5.

For strain rate localization stabilized by dilatancy alone γ_{peak} is relatively insensitive to changes in the thermal diffusion lengthscale L_{thd}, provided that the gouge layer thickness is not comparable to the localized zone thickness. The critical strain γ_{peak} is an increasing function of ε so, as for the frictional rate-strengthening only system, a more effective localization limiting mechanism not only leads to wider localized shear zones, but also slows the rate at which strain localization occurs.

Since the most rapid dynamic weakening occurs at strains comparable to γ_{peak}, if the gouge layer is sufficiently thick or the slip in an event is sufficiently small then the localized zone may not fully develop. If this occurs then we expect the strength evolution to be far smoother than the example shown in Figure 8. One caveat is that it may not be possible for slip to cease during the accelerating dynamic weakening that occurs just before a fully developed localized zone is generated.

8.4. Maximum temperature rise

Strain rate localization also has a pronounced effect on the maximum temperature. Figure 11 shows the maximum temperature rise for the localized shear solution and uniform shear solution when localization is stabilized by frictional rate-strengthening alone. For the initial stages of deformation the maximum temperature rise is well described the undrained and adiabatic solution from *Lachenbruch* [1980]. However, as the strain rate localizes the frictional heating is focused into a narrow zone, leading to a large increase in the maximum temperature rise. After straining has localized the maximum temperature rise mirrors the solution for slip on a plane, but will never converge to this solution. For the simulation shown in Figure 11 the maximum temperature rise for the localized shear solution is about three times larger than that of the uniform shear solution after a slip of 10 mm, a difference of $\sim 580°$C. Such a dramatic increase temperature rise has obvious implications for the onset of melting and the triggering of other temperature controlled dynamic weakening mechanisms such as thermal decomposition. Varying the gouge properties we find that the most rapid rises in the maximum temperature correspond to the lowest values of W_{rsf}, as would be expected since lower values of W_{rsf} means straining is confined to a narrower zone.

While the maximum temperature rise for the localized shear solution is much larger than that of the uniform shear solution, the temperature anomaly that might be observed in fault drilling studies would be smaller. This is because the temperature rise observed during drilling is controlled by the total dissipation,

$$\int_0^D \tau(\delta) \mathrm{d}\delta, \qquad (66)$$

where δ is slip and D is the total slip in an event. The rapid weakening that accompanies localization means that the total dissipation for the localized shear solution will be less than the total dissipation for the uniform shear solution, leading to a lower temperature anomaly.

We can understand the apparent contradiction between a higher maximum temperature rise and a lower temperature anomaly by realizing that the extremely small width of the localized zone means that the maximum temperature rise will rapidly decay after the cessation of slip. The timescale for decay of the localized peak in temperature can be estimated by W_{rsf}^2/α_{th}. Using our predictions of localized zone thickness we predict decay timescales between 0.022 and 3.6 milliseconds. The very short decay time may be important when estimating the maximum temperature rise on a fault using thermal maturity methods *Polissar et al.* [2011], with narrower localized zones corresponding to a larger estimate for the temperature rise.

9. Conclusions

In this paper we have used numerical simulations to study strain rate localization in a fluid-saturated gouge material undergoing thermal pressurization. Two stabilizing mechanisms were considered to prevent the deformation collapsing onto a mathematical plane, frictional rate-strengthening and dilatancy. We predict a localized zone thickness, which is compared with the predictions for localized zone thickness from the companion paper *Rice et al.* [2013], and show the impact localization has on the maximum temperature rise and shear strength evolution.

For frictional rate-strengthening alone the strain rate profile has a Gaussian shape throughout the deformation allowing us to infer the width of the localized zone W_{rsf}. The peak localized zone thickness is found to be almost independent of the gouge layer thickness. A parameter sweep leads to a formula for the localized zone thickness as a function of the gouge properties, and the thickness is set by a balance between thermal pressurization, hydrothermal diffusion and rate-strengthening friction. For parameters modeling a

depth of 7 km we predict localized zone thicknesses between 4 μm and 44 μm.

For dilatancy alone we also predict a localized zone thickness that is independent of the gouge layer thickness. A parameter sweep leads to a formula for the localized zone thickness W_{dil} as a function of the gouge parameters, with the formula given in equation (50). Using this formula we predict localized zone thicknesses between 1 μm and 2 μm at a depth of 7 km. The most sensitive dependence of W_{dil} is on ε, which models the magnitude of dilatancy.

Strain rate localization has a dramatic effect on the strength and temperature evolution of the gouge layer. As straining localizes the frictional heating is focused into a narrower zone, leading to a much larger temperature rise than that predicted if localization is neglected. This focusing of frictional heating also leads to rapid thermal pressurization and the development of a localized shear zone coincides with a significant strength drop.

Finally, we tested the hypothesis in *Rice* [2006] that inertial effects across the gouge layer will be unimportant during shear. We found that in general inertial effects across the gouge layer will be unimportant in both real earthquakes and high-velocity friction experiments, but may play a role very close to the tip of a dynamically propagating rupture or when the pore pressure approaches the normal stress on the fault.

References

Andrews, D. J. (2002), A fault constitutive relation accounting for thermal pressurization of pore fluid, *Journal of Geophysical Research*, 107, B12, 2363, doi:10.1029/2002JB001942.

Blanpied, M. L., C. J. Marone, D. A. Lockner, J. D. Byerlee, and D. P. King (1998), Quantitative measure of the variation in fault rheology due to fluid-rock interactions, *Journal of Geophysical Research*, 103, 9691-9712.

Brantut, N., A. Schubnel, J.-N. Rouzaud, F. Brunet, and T. Shimamoto (2008), High-velocity frictional properties of a clay-bearing fault gouge and implications for earthquake mechanics, *Journal of Geophysical Research*, 113, B10401, doi:10.1029/2007JB005551.

Chester, F. M., and J. S. Chester (1998), Ultracataclasite structure and friction processes of the Punchbowl Fault, San Andreas System, California, *Tectonophysics*, 295, 199-221.

Chester, J. S., A. K. Kronenberg, F. M. Chester, and R. N. Guillemette (2003), Characterization of natural slip surfaces relevant to earthquake mechanics, *Eos Tans. AGU*, 84 (46), Fall Meet Suppl., Abstract S42C-0185.

Chester, J.S., F. M. Chester, and A. K. Kronenberg (2005), Fracture surface energy of the Punchbowl Fault, San Andreas System, *Nature*, 437, 133-136, doi:10.1038/nature03942.

Da Cruz, F., S. Emam, M. Prochnow, J.-N. Roux, and F. Chevoir (2005), Rheophysics of dense granular materials: Discrete simulation of plane shear flows, *Physical Review E*, 72, 021309, doi:10.1103/PhysRevE.72.021309.

De Paola, N., C. Collettini, D.R. Faulkner, and F. Trippetta (2008), Fault zone architecture and deformation processes within evaporitic rocks in the upper crust, *Tectonics*, 27, TC4017, doi:10.1029/2007TC002230.

Dieterich, J. H. (1979), Modeling of rock friction 1. Experimental results and constitutive equations, *Journal of Geophysical Research*, 84, 2161-2168.

Fine, R. A., and F. J. Millero (1973), Compressibility of water as a function of temperature and pressure, *The Journal of Chemical Physics*, 59(10), 5529-5536.

Forterre, F., and O. Pouliquen (2008), Flows of dense granular media, *Annual Reviews of Fluid Mechanics*, 40, 1-24, doi: 10.1146/annurev.fluid.40.111406.102142.

Garagash, D.I. (2012), Seismic and aseismic slip pulses driven by thermal pressurization of pore fluid, *Journal of Geophysical Research*, 117, B04314, doi:10.1029/2011JB008889.

Kitajima, H., J. S. Chester, F. M. Chester, and T. Shimamoto (2010), High-speed friction of disaggregated ultracataclasite in rotary shear: Characterization of frictional heating, mechanical behavior, and microstructure evolution, *Journal of Geophysical Research*, 115, B08408, doi:10.1029/2009JB007038.

Lachenbruch, A. H. (1980), Frictional heating, fluid pressure, and the resistance to fault motion, *Journal of Geophysical Research*, 85, 6097-6112.

Likhachev, E. R. (2003), Dependence of water viscosity on temperature and pressure, *Technical Physics*, 48(4), 514-515, doi: 10.1134/1.1568496.

Marone, C., C. B. Raleigh, and C. H. Scholz (1990), Frictional behavior and constitutive modeling of simulated fault gouge, *Journal of Geophysical Research*, 95, 7007-7025.

Mase, C. W., and L. Smith (1985), Pore-fluid pressures and frictional heating on a fault surface, *Pure and Applied Geophysics*, 122, 583-607.

Mase, C. W., and L. Smith (1987), Effects of frictional heating on the thermal, hydrologic, and mechanical response of a fault, *Journal of Geophysical Research*, 92, 6249-6272.

Mizoguchi, K., T. Hirose, T. Shimamoto, and E. Fukuyama (2009), High-velocity frictional behavior and microstructure evolution of fault gouge, obtained from Nojima fault, soutwest Japan *Tectonophysics*, 471, 285-296, doi:10.1016/j.tecto.2009.02.033.

Noda, H., E. M. Dunham, and J. R. Rice (2009), Earthquake ruptures with thermal weakening and the operation of major faults at low overall stress levels, *Journal of Geophysical Research*, 114, B07302, doi:10.1029/2008JB006143.

Polissar, P. J., H. M. Savage, and E. E. Brodsky (2011), Extractable organic material in fault zones as a tool to investigate frictional stress, *Earth and Planetary Science Letters*, 439-447, doi:10.1016/j.epsl.2011.09.004.

Reches, Z., A. S. Madden, and X. Chen (2012), Fault gouge rheology under confined, high-velocity conditions, Abstract T21C-2590 presented at 2012 Fall Meeting, AGU, San Francisco, Calif. 3-7 Dec.

Rempel, A. W., and J. R. Rice (2006), Thermal pressurization and onset of melting in fault zones, *Journal of Geophysical Research*, 111, B09314, doi:10.1029/2006JB004314.

Rice, J. R. (2006), Heating and weakening of faults during earthquake slip, *Journal of Geophysical Research*, 111, B05311, doi:10.1029/2005/JB004006.

Rice, J.R, J.W. Rudnicki, and J. D. Platt (2013), Stability and localization of rapid shear in fluid-saturated gouge, 1. Linearized stability analysis, *submitted*.

Segall, P., and J. R. Rice (1995), Dilatancy, compaction, and slip instability of a fluid-infiltrated fault, *Journal of Geophysical Research*, 100, 22,155-22,171.

Smith, S. A. F., G. Di Toro, S. Kim, J.-H. Ree, S. Nielsen, A. Billi, and R. Spiess (2013), Coseismic recrystallization during shallow earthquake slip, *Geology*, 41, 63-66, doi: 10.1130/G33588.1.

Sulem, J., and V. Famin (2009), Thermal decomposition of carbonates in fault zones: Slip-weakening and temperature-limiting effects, *Journal of Geophysical Research*, 114, B03309, doi:10.1029/2008JB006004.

Sulem, J., I. Stefanou, and E. Veveakis (2011), Stability analysis of undrained adiabatic shearing of a rock layer with Cosserat microstructure, *Granular Matter*, 13, 261-268, doi:10.1007/s10035-010-0244-1.

Vardoulakis, I. (2002), Dynamic thermo-poro-mechanical analysis of catastrophic landslides, *Géotechnique*, 52, 157-171, doi:10.1680/geot.2002.52.3.157.

Wibberley, C. A. J., and T. Shimamoto (2003), Internal structure and permeability of major strike-slip fault zones: The Median Tectonic Line in Mie Prefecture, southwest Japan, *Journal of Structural Geology*, 25, 59-78.

J. D. Platt, School of Engineering and Applied Sciences, Harvard University, 327 Pierce Hall, 29 Oxford Street, Cambridge, MA 02138, USA. (jplatt@seas.harvard.edu)

J.W. Rudnicki, Department of Mechanical Engineering and Department of Civil and Environmental Engineering, Northwestern University, Room A333, 2145 Sheridan Road, Evanston, IL 60208, USA. (jwrudn@northwestern.edu)

J. R. Rice, Department of Earth and Planetary Sciences and School of Engineering and Applied Sciences, Harvard University, 224 Pierce Hall, 29 Oxford Street, Cambridge, MA 02138, USA. (rice@seas.harvard.edu)